Brittle-Ductile Deformation and Tensile Rupture of Dome Lava During Inflation at Santiaguito, Guatemala

Adrian J. Hornby[1,2] iD, Yan Lavallée[1] iD, Jackie E. Kendrick[1] iD, Silvio De Angelis[1] iD, Anthony Lamur[1] iD, Oliver D. Lamb[1,3] iD, Andreas Rietbrock[1,4], and Gustavo Chigna[5]

[1]Department of Earth, Ocean and Ecological Sciences, University of Liverpool, Liverpool, UK, [2]Department für Geo- und Umweltwissenschaften, Ludwig-Maximilians-Universität München, Munich, Germany, [3]Department of Geological Sciences, University of North Carolina at Chapel Hill, Chapel Hill, NC, USA, [4]Geophysikalisches Institut (GPI), Karlsruhe Institut für Technologie, Karlsruhe, Germany, [5]Instituto Nacional de Sismologia, Vulcanologia, Meteorologia e Hydrologia (INSIVUMEH), Guatemala City, Guatemala

Abstract Gas-and-ash explosions at the Santiaguito dome complex, Guatemala, commonly occur through arcuate fractures, following a 5- to 6-min period of inflation observed in long-period seismic signals. Observation of active faults across the dome suggests a strong shear component, but as fault propagation generally proceeds through the coalescence of tensile fractures, we surmise that explosive eruptions require tensile rupture. Here, we assess the effects of temperature and strain rate on fracture propagation and the tensile strength of Santiaguito dome lavas. Indirect tensile tests were conducted on samples with a porosity range of 3–30% and over diametral displacement rates of 0.04, 0.004, and 0.0004 mm/s. At room temperature, the tensile strength of dome rock is rate independent (within the range tested) and inversely proportional to the porosity of the material. At eruptive temperatures we observe an increasingly ductile response at either higher temperature or lower displacement rate, where ductile deformation is manifest by a reduction in loading rate during constant deformation rate tests, resulting in slow tearing, viscous flow, and pervasive damage. We propose a method to conduct indirect tensile tests under volcanic conditions using a modification of the Brazilian disc testing protocol and use brittleness indices to classify deformation modes across the brittle-ductile transition. We show that a degree of ductile damage is inevitable in the lava core during explosions at the Santiaguito dome complex and discuss how strain leading to rupture controls fracture geometry, which would impact gas pressure release or buildup and regulate explosive activity.

Plain Language Summary Using instruments we installed at Santiaguito, an active lava dome complex in Guatemala, we detected repeating cycles of inflation and deflation. The inflation took less time leading up to explosions compared to weak gas puffing, which led us to suspect that lava breaking and flowing might be responsible. To investigate this, we made laboratory tests where we put lava samples under tension, which is the most common way they break. We ran tests where we squeezed lavas at faster and slower rates in a press, and we also heated the lavas to their eruption temperatures—about 800 °C—for some tests. Since the lavas contain volcanic glass, in some high temperature tests the glass partially flowed. In other tests the lavas were completely brittle, which means they stored up stress and then broke without flowing. The lava's behavior depends on the temperature and how fast they are squeezed. Finally, we considered how fast dome lavas at Santiaguito would have to be deformed to either break or stay intact during inflation of the dome. This study gives us a better idea of how dome lavas deform and how that affects hazardous activity during eruptions.

1. Introduction

1.1. Vulcanian Activity at Active Lava Domes

The processes triggering "vulcanian" gas-and-ash explosions at active lava domes remain widely debated as competing hypotheses exist at both all-encompassing (Chouet et al., 2005) and volcano-specific (Hall et al., 2015) scales. Vulcanian events have been attributed to a range of processes, from the ascent of a fresh batch of bubbly magma in the shallow conduit (Cassidy et al., 2015) and gas pressure accumulation due to fracture sealing (Kendrick et al., 2016; Okumura & Sasaki, 2014) healing (Gardner et al., 2018; Lamur et al., 2019) and cyclic gas fluxing (Michaut et al., 2013) to the development of shear fractures along the margins of volcanic

conduits during ascent of highly viscous magma (Lavallée et al., 2015; Lensky et al., 2008; Tuffen et al., 2003). On the other hand, there is a general agreement on the processes that result in fracturing of parts of the dome during explosive activity to allow the ejection of ash-laden plumes. The rupture of materials under low confining pressure (i.e., at shallow depths where the magmastatic or lithostatic pressure exerted by the overburden is low) commonly proceeds via the nucleation, propagation, and coalescence of tensile fractures, even under compressive stresses (Heap et al., 2015; Kilburn, 2003; Paterson & Wong, 2005) unless conditions for supershear (i.e., super-Rayleigh) rupture are met (Xia et al., 2004), possible in some scenarios (Lavallée et al., 2012). A detailed investigation of the tensile strength of dome materials at eruptive conditions is therefore key to understanding the processes controlling explosive activity at lava dome volcanoes. In recent years, several well-monitored lava dome volcanoes have provided a wealth of geophysical data that are rapidly changing our understanding of eruption mechanisms. The integration of seismic and tilt signals has proven helpful to track pressure evolution during dome eruptions (Chouet & Matoza, 2013; Johnson et al., 2014; Thomas & Neuberg, 2014; Voight et al., 1998). Seismicity provides evidence for magma fracturing (Bean et al., 2014; Lamb et al., 2017; Neuberg et al., 2006) and gas flux (Chouet, 1988; Matoza et al., 2015) during transitions to explosive activity, while proximal monitoring of tilt signals at dome volcanoes has identified shallow (<500 m) inflation for several minutes prior to vulcanian explosions (Johnson et al., 2014; Lyons et al., 2012; Nishimura et al., 2012). Such inflation signals may indicate pressurization of shallow magma due to gas fluxing (Johnson et al., 2014; Michaut et al., 2013) or magma ascent and wall rock traction (Albino et al., 2011; Neuberg et al., 2018) or a combination of the two (Lavallée et al., 2015; Lensky et al., 2008). Both gas pressurization (e.g. Alidibirov & Dingwell, 1996) and strain localization during shear (Lavallée et al., 2013; Massol & Jaupart, 2009; Papale, 1999; Thomas & Neuberg, 2012; Wallace et al., 2019) may cause the propagation of tensile fractures.

1.2. Volcanic Activity at the Santiaguito Dome Complex, Guatemala

Volcanism at Santiaguito began in 1922 in the crater formed during the 1902 Plinian eruption of Santa Maria volcano (Figures 1a–1c). Over the last 100 years, eruptive activity has remained remarkably constant within the Santiaguito dome complex, undergoing cycles of effusion and explosive activity across four vents and over varying timescales (Harris et al., 2003; Rhodes et al., 2018; Scott et al., 2013). The Santiaguito dome complex is located in the Western Highlands of Guatemala, at the Northern end of the Central American volcanic arc stretching from Guatemala to Panama (Figure 1b). The volcanic arc runs parallel to the trench formed from the subduction of the Cocos plate and consists of hundreds of volcanoes along the active front, as well as dozens of monogenetic back-arc volcanoes (Eiler et al., 2003; Walker et al., 2011). Since the 1970s, eruptions at Santiaguito have been located at the Caliente vent, characterized by effusion of lava flows accompanied by gas-and-ash explosions from a 200-m-wide dome, producing small to moderate ash-poor clouds every 20–200 min (Bluth & Rose, 2004; Harris et al., 2003; Patrick, 2007). Visual observations between 2012 and early 2015 showed that the shallow dome structure in the Caliente vent remained mostly intact during explosions, and magma effusion fed lava flows that descended the south and southeast flanks (Figure 1). Lava flows were active for most of this period; however, effusion rate declined through 2014, ceasing in December. From late 2015–2016, the long-term eruptive behavior at Santiaguito underwent a transition to more powerful and less frequent explosions, producing plumes up to 8 km high, destroying the summit dome and forming a deep crater in the Caliente vent (Lamb et al., 2019). From late 2016 onward, the activity has returned to the long-term behavior. In recent years, geophysical monitoring campaigns have shown that the long-term, predominantly weak explosive activity is accompanied by repetitive "inflation-deflation" cycles over ~26 min, as monitored by long-period seismic and tilt signals (Johnson et al., 2014; Sanderson et al., 2010). The culmination of the inflation phases at Santiaguito results in either an outgassing event or a gas-and-ash explosion (Lavallée et al., 2015), where the latter outcome is accompanied by inflation occurring at higher rates, as well as by the occurrence of a very long period seismic event (Johnson et al., 2014). The shallow magmatic system thus resides in a delicate yet repeatable balance between pressurization, fracturing events, and outgassing regimes, where the rate and timescale of deformation ultimately determine the eruptive style (cf. Lavallée et al., 2015).

1.3. Failure Modes and Eruption Triggers at Santiaguito

Typical explosive activity at Santiaguito is characterized by low eruption magnitudes and plume volumes (De Angelis et al., 2016; Patrick, 2007; Scharff et al., 2014) that indicate open vent activity and a nondestructive
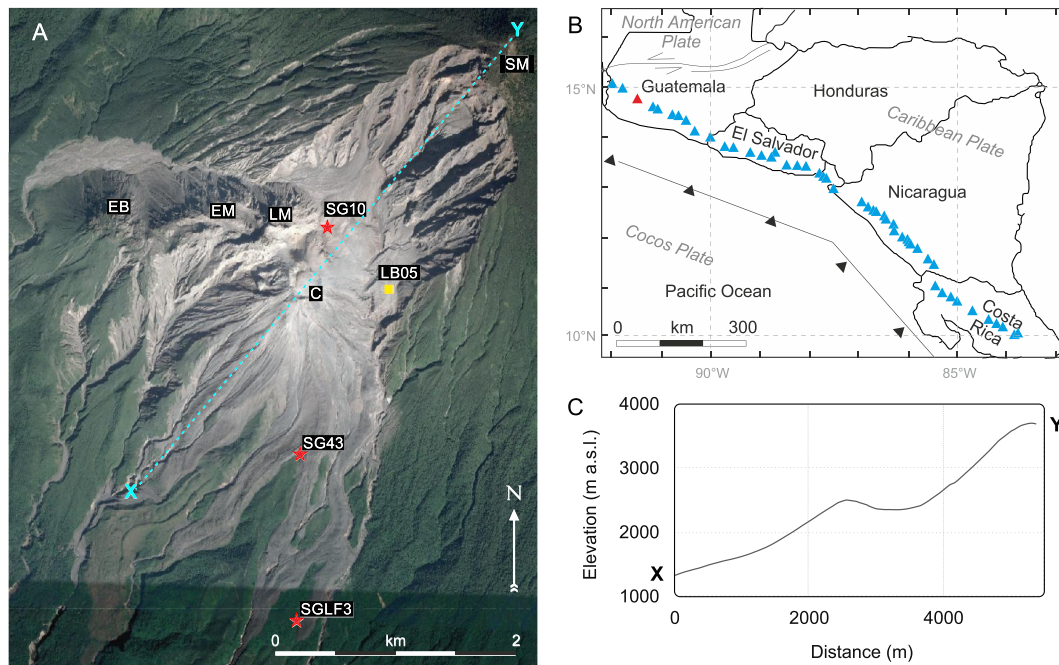
Figure 1. Location and tectonic setting of the Santiaguito dome complex. (a) Satellite imagery showing the active domes (EB, El Brujo; EM, El Monje; LM, La Mitad; C, Caliente) and Santa Maria (SM) volcano. The sampling localities are shown by red stars with the sample code. Recent lava flows erupted from Caliente were sampled (SG43 and SGLF3) as well as a large bomb (SG10) and a dense, glassy block (SGPF13) that was collected from a pyroclastic flow deposit 2 km south of the 2014–2015 lava flow (see Table 1 for details). The location of seismic and infrasound station LB05 is shown as a yellow square. Image: Google-CNRS-Airbus-Digital Globe. (b) Subduction of the Cocos plate forms a parallel chain of volcanoes along the active front of the Central America volcanic arc. The Santiaguito dome complex is shown as a red triangle, with other major volcanoes shown in blue. Modified from several maps (Eiler et al., 2003; Escobar-Wolf, 2010; Scott et al., 2012). (c) Topography along the section *X-Y*, marked on panel (a) in cyan.

source of magma pressurization and depressurization. The general preservation of the dome structure following explosions along fractures suggests that critical gas overpressure does not develop readily across the whole dome prior to vulcanian explosions at Santiaguito. There are complementary lines of evidence to support this hypothesis. A purely gas-driven tilt signal is opposed by observations that SO_2 outgassing fluxes do not significantly vary during preeruptive and posteruptive episodes and show poor correlation with eruption magnitudes (Holland et al., 2011; Rodríguez et al., 2004). In addition, Okumura and Sasaki (2014) estimated that the timescale of permeability reduction due to healing of fractures at Santiaguito is at least 1 order of magnitude longer than the eruption interval, suggesting that gas overpressures sufficient to exceed the tensile strength of magma could not develop throughout the shallow magma. Finally, typical explosion plumes are weak and ash poor (De Angelis et al., 2016; Esse et al., 2018; Patrick, 2007) and the volcanic ash particles emitted during explosions are dense and blocky, with few small vesicles and no evidence for bubble wall breakage (Hornby et al., 2019; Rose et al., 1980), indicating that the erupted material has a low bubble number density and does not fail due to bulk bubble overpressure alone. Therefore, it is likely that localized rupture causes transient permeability shifts, possibly promoted by strain in marginal shear zones, providing an important contribution to the triggering of explosions and the cyclic tilt patterns.

Modeling of the inflation-deflation cycles by a gas pressurization source (Johnson et al., 2014) at depths of 100–600 m (Sahetapy-Engel et al., 2008; Sanderson et al., 2010) has been proposed and requires highly permeable pathways (i.e., fractures connecting a pressurized region to the dome surface) during an explosion. At such shallow depths and under low confining pressure, tensile fractures are likely to dominate. We anticipate that upon formation of a throughgoing tensile fracture, the differential residual stress may be dissipated by slip along faults. Shear motion is observed during explosions as the dome surface rises and falls by 0.5 m in 1 s, (Johnson et al., 2008) indicating the faulting and slip of conduit magma at velocities ~1 m/s. Previous work has argued that slip of a magma plug is controlled by frictional properties at the slip

interfaces (Hornby et al., 2015; Kendrick et al., 2014; Lavallée et al., 2012) and that slip generates rapid temperature increases sufficient to induce melting as well as local vesiculation in the fault zone during the piston dynamics of the active Caliente dome at Santiaguito (Lavallée et al., 2015). Lavallée et al. (2015) argue that the pore pressure developed in the shallow magmatic column is insufficient to trigger wholesale fragmentation but local tensile failure only; they present a model in which thermal vesiculation due to shear heating along fault zones generates the pore pressures capable of triggering partial fragmentation. They reason that comminution and local fragmentation generated by faulting, even for only a few centimeters of slip (Hornby et al., 2015; Kendrick et al., 2014), may significantly weaken the magma adjacent to the fault and create fracture space to allow the dome structure to deform during inflation-deflation cycles, thus increasing its overall structural stability. Such "sacrificial" fragmentation (De Angelis et al., 2016; Lavallée et al., 2015) may regulate dome structures over recurrent tilt cycles. Volcanic ash produced in such a cataclastic and thermal-driven fashion may further encourage pulsatory ash emission dynamics (Scharff et al., 2014) and create ash particles with a distinct mineralogical and physical signature (Hornby, Lavallée, Kendrick, Rollinson, et al., 2019; Lavallée et al., 2015; Rose et al., 1980).

1.4. Tensile Strength and the Development of Tensile Fractures

A common element of dome eruption models is the requirement for excursions of magma into the brittle deformation regime. Vulcanian explosions require magmatic fragmentation (Dingwell, 1996); in addition, ascent-driven rupture of magma where strain localizes (e.g., De Angelis & Henton, 2011; Lensky et al., 2008; Papale, 1999) may lead to the development of shear and tensile fracture networks at the margins of the conduit (Sparks, 1997; Tuffen et al., 2003; Massol & Jaupart, 2009; Rhodes et al., 2018), which may be followed by progressive fracture healing (e.g., Lamur et al., 2019) in a process which can repeat multiple times during magma ascent (Tuffen et al., 2003). Finally, lava may break in tension due to the action of progressive cooling contraction of the dome carapace (Lamur et al., 2018; Suzuki-Kamata et al., 2009; Wadge et al., 2009). In all of these cases (even for the development of shear zones) failure initiates in tension (Stanchits et al., 2006).

Until recent years, the mechanics of volcanic rocks and magma in tension has received relatively little attention, focusing on fragmentation by pore overpressure (e.g., Spieler et al., 2004), high-temperature fracture toughness (Balme et al., 2004), and tensile failure of country rock (Benson et al., 2012; Parisio et al., 2019). This comes despite longstanding recognition of the paucity of low pressure–high temperature tensile strength data and their importance to our understanding of the mechanics of volcanic eruptions (Rocchi et al., 2003; Self et al., 1979; Shaw, 1980). A spate of recent studies has improved this situation, comprising high-temperature tensile strength experiments during the development of columnar jointing (Lamur et al., 2018) and fracture healing (Lamur et al., 2019) as well as room temperature tensile tests on andesites from Rotokowa and Mount Taranaki in New Zealand (Siratovich et al., 2012; Zorn et al., 2018), Soufrière Hills Volcano in Montserrat (Harnett et al., 2019), Volcán de Colima in Mexico (Lamb et al., 2017), and a range of volcanic rocks from the Krafla geothermal system in Iceland (Eggertsson et al., 2018).

Indirect tensile strength tests, or Brazilian disc tests, are the most commonly employed method to study material failure in tension (Li & Wong, 2013). The tests, generally conducted at a single, fixed displacement rate and at ambient temperature, provide evidence for material strength decreasing with increasing porosity and indicate that tensile strength is approximately 10–20 times lower than compressive strength (Harnett et al., 2019; Lamb et al., 2017; Perras & Diederichs, 2014; Zorn et al., 2018). However, the range of typical test conditions cannot be easily applied to active volcanoes, which take place at high temperature and at widely varying strain rates, and which may result in brittle failure as well as in ductile and viscous deformation (Lavallée et al., 2007; Rocchi et al., 2003). Herein, we address this important data gap by testing the behavior of dome materials from the Santiaguito dome complex at conditions simulating natural conduit temperatures and strain rates, and we propose a protocol to conduct indirect tensile strength tests at elevated temperature.

2. Experimental Setup and Data Collection

2.1. Visual and Geophysical Monitoring of Activity at Caliente

In November 2012, November–December 2014 and April 2015, we visited the Santiaguito dome complex, sampled eruptive products and made visual observations of the eruptive activity from a vantage point on

Santa Maria volcano. During November 2014, we deployed a network of five broadband seismometers, six short-period seismometers, and six infrasound microphones around the Santiaguito dome complex (De Angelis et al., 2016; Lamb et al., 2019). Here, we analyzed very long period seismic signals (600–30 s) from a Trillium compact broadband seismometer at station LB05 (14°44′18″N, 91°33′38″W), ~500 m NW, and 200 m below the active Caliente vent at Santiaguito (Figure 1a). Following recent studies (De Angelis & Bodin, 2012; Johnson et al., 2009, 2014), we used the horizontal component of very long period signals to recover ground tilt. Infrasound was recorded using an iTem broadband infrasound microphone colocated at station LB05.

2.2. Material

Four pristine dome rocks were collected during field campaigns in 2012, 2014, and 2015 at the active Caliente dome. Sampling locations together with the sample codes are reported in Figure 1 and Table 1. Lava flow samples (SG43 and SGLF3) were collected from the base of the flow levees, and a fresh airfall bomb (SG10) was collected from the base of Caliente, while the block collected from a pyroclastic flow (SGPF13) had traveled a considerable distance from the source. The rocks are dacites with rhyolitic interstitial glass chemistry and mineralogical assemblage consistent with observations from Scott et al. (2013); however, the rocks vary in porosity, as determined by He-pycnometry measurements using a 100 cm^3 chamber in an AccuPyc 1340 Automatic Gas Pycnometer from Micromeritics. The mineralogical assemblage is composed of ~50 vol.% plagioclase feldspar (phenocrysts and microlites) with 5–6 vol.% Mg pyroxenes, 2 vol.% amphibole, and minor Ti-magnetite, Ilmenite, and crystalline silica (Hornby, Lavallée, Kendrick, Rollinson, et al., 2019; Scott et al., 2013). The remainder interstitial glass hosts microlites of plagioclase and iron oxides. Image analysis of photomicrographs shows that phenocrysts form 36–40 area % of the samples, with mean aspect ratios of 1.8 ± 0.25 (see Table 1).

2.3. Softening Temperature Determination

To constrain the flow temperature regime of these lavas, we measured the softening temperature, using a Netzsch TMA 402F1 Hyperion thermomechanical analyzer. For these tests, we prepared 6-mm × 5-mm cores of each sample. Each core was axially loaded in a piston assembly, under a load of 3 N (±0.01 mN) and heated at 3 °C/min while monitoring the change in sample height at a resolution of ±0.125 nm. During heating, the samples expand and viscous flow of the groundmass glass above the glass transition temperature (T_g) causes the sample to begin to axially compact. The softening point was constrained as the temperature at the inflection point where the samples began to compact, and the measurement was stopped when the sample shortened by a strain of 0.25% under the imposed load.

2.4. Indirect Tensile Tests

For indirect tensile testing, rock samples were cored into discs of 39.8 ± 0.1 mm diameter and 20 ± 2-mm thickness, giving a thickness:diameter ratio of approximately 0.5, meeting ASTM specifications (ASTM, 2004) and as independently recommended (Lin et al., 2016; Wei & Chau, 2013). Prior to testing, porosities (Φ) of each core were measured by He-pycnometry (Section 2.2, Table 2). Indirect tensile strength tests were conducted using an Instron 1362 servo-driven uniaxial press with a 100-kN load cell.

The samples were loaded so that force was applied diametrically, with the curved disc edge against the flat, parallel platens of the press, thereby imposing a tensile stress on the sample interior (Perras & Diederichs, 2014). This configuration conforms to ASTM specifications, and an independent study has shown it to produce a valid stress field (Markides & Kourkoulis, 2016). ASTM specifications specify that a Brazilian tensile strength measurement must be conducted within the stressing rate of 3 to 21 MPa/min, achieving failure within 1–10 min, though the ISRM guidelines propose a loading rate of 0.2 kN/s, which comes to approximately 9.5 MPa/min for the sample geometry used here, and specify a failure time of 15–30 s (ASTM, 2004; ISRM, 1978; Newman & Bennett, 1990). Given this dichotomy in failure time and that previous studies have found an influence of deformation on loading rate (Gong et al., 2019; Newman & Bennett, 1990), here we conduct tests at variable displacement rates of 0.04, 0.004, and 0.0004 mm/s and measured sample temperatures (T_s) of 25 °C, 752.4 ± 11.3 °C, and 800.8 ± 12 °C (note that, for the sake of brevity, we refer to these as three sets of tests at sample temperatures of 25, 750, and 800 °C hereafter) to examine the effect of rate on the ductile-brittle response of a suite of variably porous rocks. Failure time and loading rate for room temperature tests conducted at 0.004 mm/s meet the standards to be termed a Brazilian tensile test.

Table 1
Description and Location of Samples Used, Together With Textural Characterization and Softening Point Temperature, Which Is Analogous to the Glass Transition Temperature, T_g, in These Glass-Bearing Volcanic Rocks

Sample	Type	Location	GPS coordinates	Porosity Φ (%)[a]	Phenocryst (DRE fraction)[b]	Average phenocryst aspect ratio	Softening point, T_g (°C)
SG10	Fresh lava bomb (Nov 2012)	Base of Caliente	14°44′35″N 19°34′00″W	23.2–26.0	38%	1.55	740
SG43	Block from 2011–2012 lava flow	Finca El Faro	14°43′19″N 91°34′23″W	8.6–10.6	–	–	748
SGLF3	Block from 2014 lava flow	Finca San Jose Patzulin	14°42′48″W 91°34′06″W	6.1–7.7	40%	1.62	784
SGPF13	Block from pyroclastic flow	Finca El Faro	14°41′08″W 91°34′44″N	2.2–4.7	36%	2.04	786

[a]Porosity range from all tested cores.   [b]Dense Rock Equivalent (DRE).

Displacement was recorded along the vertical diametral axis of the sample and is used as a relative measure for orthogonal diametral expansion or tensile strain. In order to avoid confusion with direct tensile strain (not derived in this experimental geometry), we refer to these strain measurements as diametral strain, ε_d, and accordingly to the rate as diametral strain rate (where the displacement rates 0.04, 0.004, and 0.0004 mm/s correspond to diametral strain rates ($\dot{\varepsilon}_d$) of 10^{-3}, 10^{-4}, and 10^{-5} s^{-1}, respectively). During tests, the resultant applied force was monitored by a load cell at 100 Hz until sample failure or until a maximum of ~0.025 diametral strain (or 1-mm axial compression). The tensile stress, σ_t, reported for samples undergoing brittle deformation was calculated using

$$\sigma_t = \frac{2P}{\pi DL},\tag{1}$$

where P is the applied force (N), D is the sample diameter (m), and L is sample thickness (m).

The press was fitted with a three-zone split cylinder furnace from Severn Thermal Solutions, capable of heating samples to temperatures of ≤1,000 °C. During high-temperature tests, the furnace was heated 3 °C/min to set point temperatures of 800 and 850 °C (corresponding to sample temperatures of approximately 750 and 800 °C, respectively) and left to thermally equilibrate over a period of ~1 hr; T_s was monitored using a K-type thermocouple. The compliance of the uniaxial press was measured up to 100 kN at room temperature and at furnace temperatures of 800 and 850 °C, and an analytical solution for machine compliance described by Gruber (2018) was used to model the nonlinearity of the compliance curve. The function combines the linear elastic displacement and nonlinear displacement due to machine compliance, using empirical fitting parameters to calculate the nonlinear displacement. The method used to calculate compliance together with fitting parameters can be found in the supporting information data (Text S1 and Table S1), and the raw data for machine compliance can be found in the online data repository (Hornby, Lavallée, Kendrick, De Angelis, et al., 2019).

3. Results

3.1. Visual and Geophysical Observations

During field campaigns, we observed gas emission events as well as gas-and-ash explosions at regular intervals of ~20–200 min. Visual observations in the daytime and at night from the vantage point of Santa Maria summit (1,200 m above the Caliente vent; Figure 1c) allowed us to see the synexplosive development of fractures on the dome surface (Figure 2). During explosions and outgassing, persistent fractures formed a complex conjugate network of radiating and concentric fractures. At the onset of an explosion, ash-poor plumes appeared first, often from concentric fractures (Figures 2a and 2b), followed several seconds later by ash-rich jets rising from more linear fractures that cut across the dome surface. The same fractures appeared to have been active as gas pathways during passive outgassing and during explosions (Figures 2c and 2d); however, ash-rich bursts often erupted along separate fractures (Figures 2b and 2d). In general, explosion plumes were ash poor (De Angelis et al., 2016; Yamamoto et al., 2008), but discrete ash-rich jets appeared to contain much

Table 2
Indirect Tensile Test Results With Sample Details and Test Conditions

Core sample	Porosity Φ (%)	Diameter, D (mm)	Thickness, h (mm)	Furnace Temp. (°C)	Sample Temp., T_s (°C)	Displacement rate (mm/s)	Peak load P_m (N)	Tensile stress at P_m (MPa)	Diametral strain at P_m	Displacement at P_m (mm)
SG43D	9.10	39.80	18.99	—	25	0.004	5,532.09	4.66	0.00466	0.186
SG10A	24.69	39.74	20.16	—	25	0.004	3,470.05	2.76	0.00440	0.175
SG10D	24.33	39.83	22.77	—	25	0.004	4,541.21	3.19	0.00420	0.167
SG43F	9.33	39.81	22.41	—	25	0.004	5,408.85	3.86	0.00426	0.169
SGLF3C	7.05	39.76	20.20	—	25	0.004	6,219.88	4.93	0.00437	0.174
SGLF3D	7.05	39.79	20.33	—	25	0.004	6,004.46	4.73	0.00379	0.151
SGPF13F	3.12	39.80	18.71	—	25	0.004	6,649.05	5.68	0.00517	0.206
SGPF13B	2.91	39.75	18.43	—	25	0.004	5,812.25	5.05	0.00535	0.213
SG43B	9.55	39.80	20.27	—	25	0.0004	5,320.45	4.20	0.00436	0.174
SG43A	9.35	39.84	19.78	—	25	0.0004	4,580.31	3.92	0.00442	0.176
SG10E	25.24	39.82	20.20	—	25	0.0004	3,740.96	2.96	0.00473	0.188
SG10C	25.14	39.82	18.01	—	25	0.0004	2,838.68	2.52	0.00374	0.149
SGLF3M	7.07	39.80	20.43	—	25	0.0004	5,504.76	4.31	0.00404	0.161
SGLF3E	7.01	39.79	20.55	—	25	0.0004	5,345.46	4.16	0.00383	0.153
SGPF13A	4.72	39.80	20.25	—	25	0.0004	5,709.24	4.51	0.00470	0.187
SGPF13D	3.27	39.76	19.15	—	25	0.0004	5,914.43	4.95	0.00490	0.195
SG10S	24.10	39.81	20.00	800	762.0	0.04	5,412.16	4.33	0.00406	0.162
SGLF3G	7.28	39.76	19.74	800	758.7	0.04	6,580.57	5.34	0.00343	0.136
SGPF13K	2.25	39.77	20.30	800	741.1	0.04	7,400.07	5.84	0.00344	0.137
SG10F	24.25	39.81	20.50	800	752.9	0.004	6,696.53	5.22	0.00366	0.146
SG43K	9.85	39.80	20.77	800	752.4	0.004	6,124.29	4.72	0.00323	0.129
SG10G	23.24	39.80	20.68	800	752.8	0.004	6,361.56	—	0.00400	0.159
SG43L	10.31	39.80	20.47	800	755.6	0.004	7,957.93	6.22	0.00473	0.188
SGPF13I	2.22	39.74	20.94	800	763.3	0.004	6,642.79	5.08	0.00423	0.168
SGPF13L	3.07	39.78	20.31	800	745.2	0.004	6,097.67	4.80	0.00362	0.144
SGLF3F	7.25	39.77	21.36	800	742.6	0.004	7,084.85	5.31	0.00338	0.134
SG43E	8.62	39.79	19.45	800	748.5	0.0004	7,496.26	6.17	0.00399	0.159
SG10L	23.29	39.80	20.54	800	763.6	0.0004	3,830.78	—	0.0104	0.414
SG10B	25.96	39.81	19.59	800	743.9	0.0004	4,131.80	—	0.00828	0.329
SGLF3L	6.71	39.82	20.60	800	744.6	0.0004	6,506.48	5.05	0.00467	0.186
SGPF13E	3.88	39.78	19.99	800	758.5	0.0004	6,083.80	4.87	0.00444	0.177
SG10K	23.75	39.77	22.19	850	791.2	0.04	8,002.85	—	0.00266	0.106
SGLF3N	7.67	39.79	20.15	850	812.8	0.04	7,373.26	5.85	0.00332	0.132
SGPF13J	3.00	39.78	20.16	850	789.2	0.04	7,557.02	6.00	0.00342	0.136
SG10H	23.35	39.79	17.99	850	804.5	0.004	5,591.17	—	0.0139	0.552
SG43P	10.80	39.81	20.26	850	788.8	0.004	7,794.41	—	0.00325	0.129
SGLF3P	6.10	39.80	20.88	850	792.6	0.004	7,067.97	—	0.00334	0.173
SGPF13G	2.60	39.79	21.59	850	812.8	0.004	8,378.44	—	0.00732	0.291
SG10J	24.25	39.79	21.31	850	796.4	0.0004	7,145.46	—	0.0113	0.452
SGLF3H	6.67	39.76	20.55	850	791.6	0.0004	6,507.01	—	0.00916	0.364
SG10N	24.60	39.81	19.45	850	795.9	0.0004	1,606.79	—	0.0248[a]	0.986[a]
SGPF13C	2.98	39.76	20.48	850	796.5	0.0004	5,157.21	—	0.256[a]	4.093[a]

Note. Samples were tested at 0.04, 0.004 and 0.0004 mm/s, corresponding to diametral strain rates of 10^{-3}, 10^{-4}, and 10^{-5} s^{-1} respectively. Where possible, tests were repeated using sample pairs with closely matching porosity. For high-temperature tests, sample temperature was monitored with a K-type thermocouple immediately prior to experiments.
[a]Experiment stopped at given strain (displacement) with no failure detected.

greater mass fractions prior to buoyant rise and mixing. Following an eruption, the dome structure remained intact, although the pattern of intensely outgassing fractures intermittently changed within the central part of the summit dome during intereruptive periods. Concentric fractures around the circumference of the dome structure (Figure 2a) remained active during all periods of activity and produced the highest heat flux (Sahetapy-Engel & Harris, 2009). Continuous degassing measured in previous years (Holland et al., 2011; Rodríguez et al., 2004) showed that the vent typically remained open during intereruptive periods.

Analysis of seismic and acoustic infrasound data recorded at a distance of 500 m from the Caliente vent shows cyclic activity. Figure 3 shows tilt signals derived from the rotated horizontal components of the
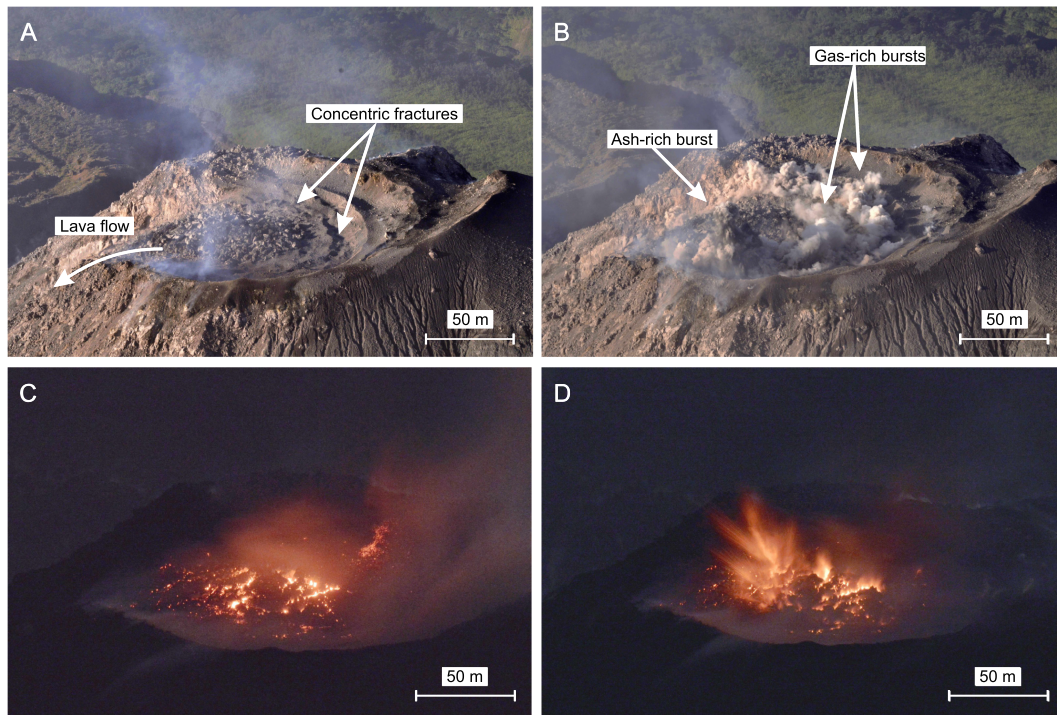
Figure 2. Photographs taken from the summit of Santa Maria, looking down on the Caliente vent. (a) The dome surface immediately prior to an explosion, showing the pattern of concentric fractures and grooves on the dome surface. (b) The onset of an explosion, showing discreet concentric fractures releasing gas, and an ash-rich burst emanating from a discreet fracture nearer to the center of the dome. (c) The dome structure at night, showing long-lived (minutes to hours) fracture traces undergoing intense outgassing. Preferential orientation of these fractures subperpendicular to the lava flow direction (to the back and left of the image) is noted. (d) The fractures in (c) are sometimes activated in subsequent explosions, as seen here. Explosions often initiate from fractures within a consistently hot central ring.

seismic record (e.g., De Angelis & Bodin, 2012) over a 6-hr period on 29 November 2014 and a 5-hr period on 4 December 2014 along with the acoustic infrasound record from a colocated microphone. Figure 3a shows 11 tilt cycles, 7 of which were accompanied by infrasound signals (each occurring at the peak of a tilt cycle) and coincident with visual observations of small gas-and-ash explosions from Caliente. Figure 3b shows nine tilt cycles, all of which were associated with explosive events. Taking a closer look into a typical tilt cycle (Figure 3b), we observe a linear increase in radial tilt (i.e., inflation) over ~5 min; following the tilt maximum, we note a rapid (<60 s) decrease in tilt, often coincident with the onset of an impulsive infrasonic signal, followed by a period of more gradual deflation lasting ~15 min. These observations, including the timescale of each tilt cycle, are in excellent agreement with those previously made by Johnson et al. (2014) and with the analysis presented in Lavallée et al. (2015), whereby 222 stacked tilt cycles recorded over 5 days revealed near-identical patterns and timescales of inflation and deflation, and showed that faster rates of inflation (positive tilt) culminated in explosions.

The data presented in Figure 3 suggest that most gas-and-ash explosions were preceded by a period of steadily increasing radial tilt over 5–6 min; here, we relate this timescale to the period of stress accumulation in the magmatic column and use it to constrain the strain rate experienced by magma leading to either passive gas emission or rupture, fragmentation, and explosion.

3.2. Tensile Strength Tests and Rupture Modes

Here we report the results of 42 indirect tensile tests conducted at ambient and volcanically relevant temperatures (Table 2) and at deformation rates of 0.04, 0.004, and 0.0004 mm/s (corresponding to $\dot{\varepsilon}_d$ of 10^{-3}, 10^{-4}, and 10^{-5} s^{-1}) on a set of variably porous volcanic rocks from Santiaguito. Mechanical data for all tests are openly available in the online data repository (Hornby, Lavallée, Kendrick, Rollinson, et al., 2019). Tests at different temperatures but deformed at a single rate and tests at a single high temperature but with different displacement rates are plotted in Figures 4a and 4b, respectively. Experiments in which the sample shows fully brittle deformation are characterized by a linear buildup of tensile stress as a function of diametral
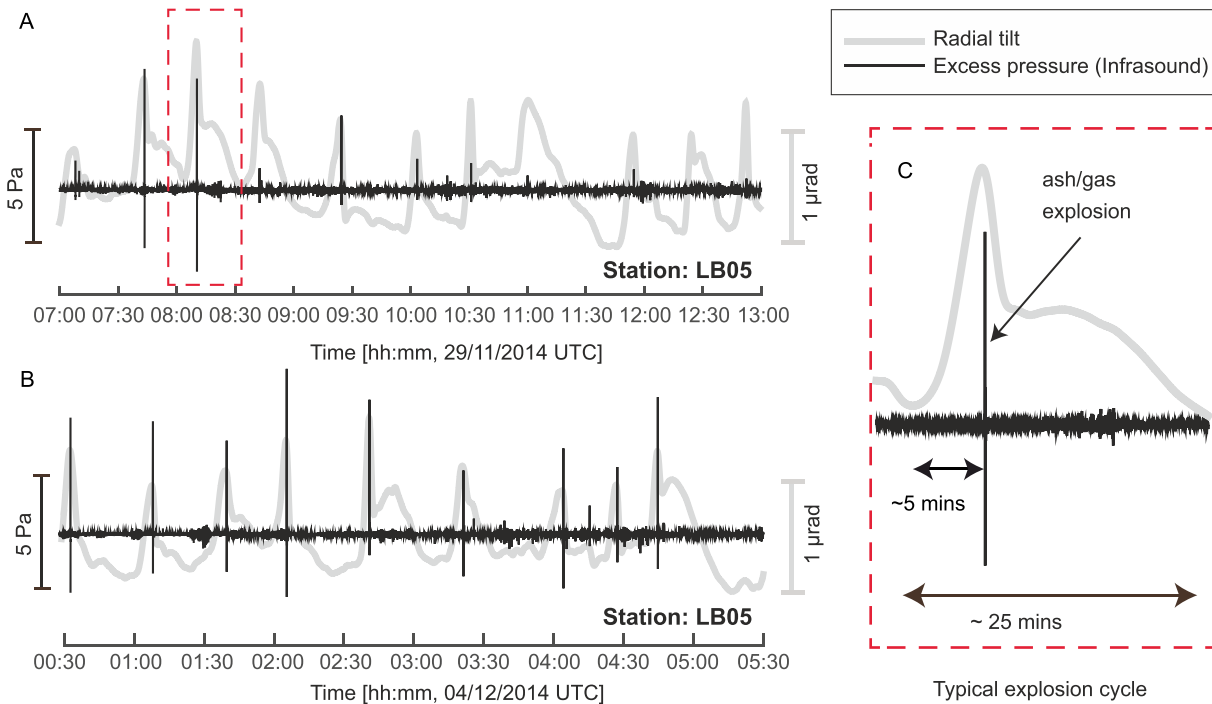
Figure 3. Geophysical data obtained during (a) a 6-hr period on 29 November 2014 and (b) a 5-hr period on 4 December 2014, showing radial tilt calculated from very long period seismic signals (thick gray line, secondary *y* axis) and infrasound (black line, primary *y* axis) monitored at station LB05, ~500 m from the active Caliente vent at Santiaguito. (c) Zoom-in of inflation-deflation cycle and infrasound pulse delimited in panel (a). Note that the timescale for inflation here is 5 min, as observed systematically prior to explosive eruptions during dome activity in 2012 (Johnson et al., 2014; Lavallée et al., 2015).

compression which results in the radial splitting of the sample and stress drop (data at 25 and 758.5 °C sample temperature in Figure 4a).

However, at higher temperature, viscous relaxation of applied stress may contribute to the deformation, leading to a nonlinear accumulation of stress with displacement as the material flows without undergoing rupture (e.g., data at $T_s = 796.5$ °C in Figure 4a). This brittle to ductile transition, met in the experiments here as temperature is increased (Figure 4a), can also be achieved by decreasing the deformation rate at a given high temperature (Figure 4b). To illustrate this phenomena, Figure 4b shows that Santiaguito lavas deformed at 797 ± 8 °C formed a well-defined macrofracture upon brittle failure (e.g., Figure 4c) at high $\dot{\varepsilon}_d$ (e.g., 10^{-3} s^{-1}); in contrast lava deformed at a lower $\dot{\varepsilon}_d$ of 10^{-4} s^{-1} led to partial stress relaxation and delayed rupture (Figure 4b), while lava deformed at 10^{-5} s^{-1} only partially tore (Figure 4d), avoiding complete rupture under the imposed strain. (Note that in the latter scenarios, the load monitored does not reflect the true tensile stress experienced by the sample as the contact area of the cylindrical sample increased due to flattening against the pistons; however, this behavior indicates the temperature and strain rate conditions at which magma can partially relax an applied stress versus accumulating stress toward material failure.) The degree of strain localization across the brittle regime (forming localized fractures; Figure 4c) and the ductile regime (pervasive deformation encouraging distributed damage and complex tearing structures; Figure 5) reflects variations in the extent of strain evidenced by the development of microstructures (i.e., crystal motion and fracture propagation) leading to rupture in magmas. Figure 5 provides evidence for incremental fracture propagation in the crenulated fracture pathways that appear to deviate between heterogeneities in the rock (e.g., crystals and pores) in high-temperature, low-deformation rate experiments. Evidence for distributed, dilatant damage within the brittle-ductile regime can be seen in Figure 5c, where radial fractures propagate inward and the tensile fracture opening increases with strain. The specific sample geometry and high strain reached in some experiments with significant ductile deformation also result in numerous radial fractures that propagate inward from the edge of the sample.

At ambient temperature, the tensile strength of the dome rocks shows an approximately linear decrease with increasing sample porosity (Figure 6a), which has a best fit following $\sigma_t = -0.99 \cdot \Phi + 5.26$. For a given
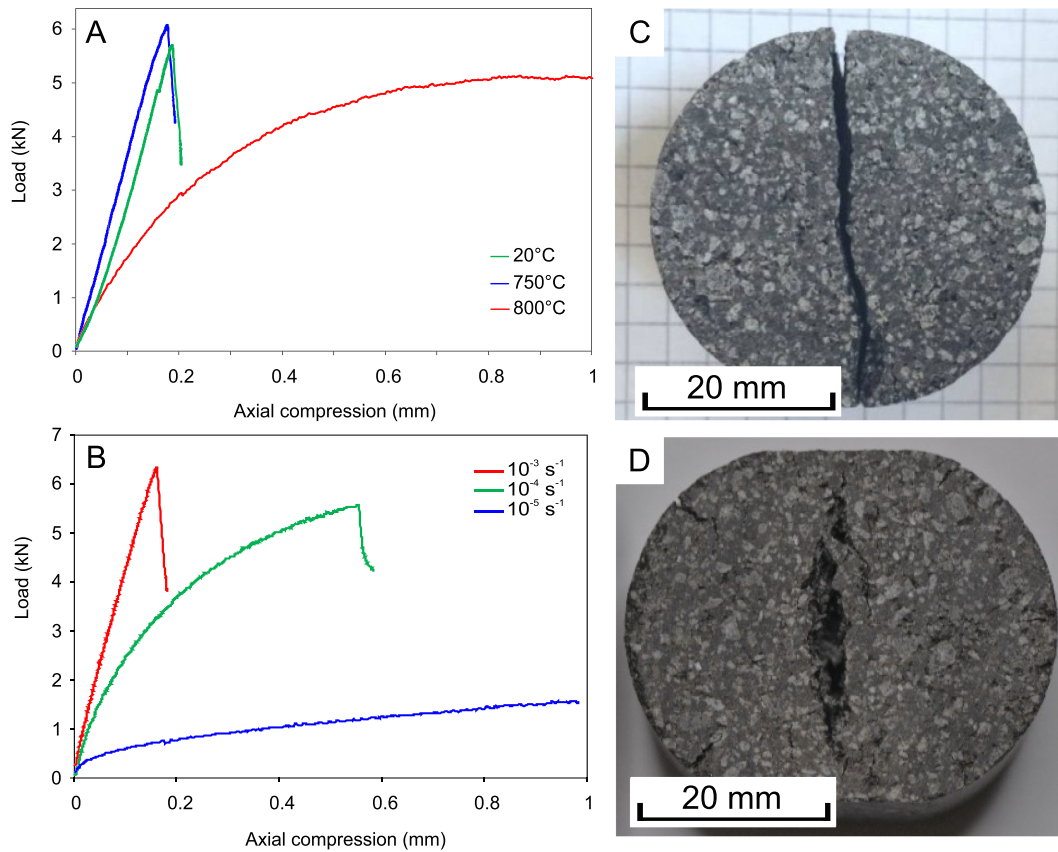
Figure 4. (a) Mechanical data for three tests using cores of rock sample SGPF13 (2.5–3% Φ) during indirect tensile tests at a $\dot{\varepsilon}_d$ of 10^{-5} s^{-1} and varying T_s of 25, 758.5, and 796.5 °C. The data show that curves at 25 and 758.5 °C (green and blue lines, respectively) are linear with a sharp drop in load at failure, typical of brittle deformation, whereas at 796.5 °C (red line) the curve is concave downward indicating relaxation of stress via increasing ductile deformation. (Note that only the first 1 mm [of 4-mm total] deformation is shown for this experiment.) The full test data can be found in the accompanying data repository. (b) Mechanical data for three tests of rock core SG10 (24–25% Φ) during indirect tensile tests at T_s of 797 ± 8 °C and different $\dot{\varepsilon}_d$ of 10^{-5}, 10^{-4}, and 10^{-3} s^{-1}. The data are nearly linear at high strain rate (red line), while tests at intermediate and low strain rate result in concave down curves. The decrease in loading rate is gradual and leads to failure in the intermediate strain rate (green line), while the curve at the lowest strain rate (blue line) shows a more acute inflexion close to the origin and lacks a stress drop indicating rupture. (c) Ruptured sample SGLF3G produced by brittle failure at 758.7 °C and a $\dot{\varepsilon}_d$ of 10^{-3} s^{-1}. Deformation is accommodated solely by the fracture, which passes through the center of the sample. (d) Partially ruptured sample SGPF13C produced at 795.9 °C and $\dot{\varepsilon}_d$ of 10^{-5} s^{-1} (blue line in B), showing a mixture of ductile deformation (evident from the flattening of parts of the disc that were in contact with the piston of the press) as well as brittle deformation evidenced by the wide crack or tear observed in the center of the sample and radial fractures propagating from the sample edges

porosity we note a variability in tensile strength, which is slightly larger at higher porosity. When deformed at high temperatures, samples' strength appeared to vary more for a given porosity (Figures 6b and 6c). (Note that in Figure 6c the hollow symbols refer to the maximum stress reached by material which did not rupture.) The porosity dependence of tensile strength observed at ambient temperature is not as strong during deformation at high temperature, where we note a shallower gradient (Figures 6b and 6c). In general, at high-temperature conditions, the tensile strength of the samples was higher than their rock counterparts for a given porosity, with important exceptions when low diametral strain rates favored viscous relaxation and flow at low accumulated stresses. While the scatter may in part obscure the effect of deformation rate, such that we cannot quantify the influence of rate between 0.004 and 0.0004 mm/s, the slowest $\dot{\varepsilon}_d$ of 10^{-5} s^{-1} resulted in the lowest σ_t at both ambient and high-temperature conditions (Figure 6).

We explore further the rate-weakening rheology of lava deformation by evaluating the total ε_d accommodated by samples during the tests (Figure 7). This analysis highlights the narrow range of ε_d at failure (i.e., ε_d at peak load) between 0.0027 and 0.0054 for deformation under fully brittle conditions, irrespective of porosity, temperature, or $\dot{\varepsilon}_d$. Samples for which $\varepsilon_d > 0.006$ accumulated lower tensile loads for a given porosity (Figure 7); this only occurred during tests at high temperature and low strain rate.
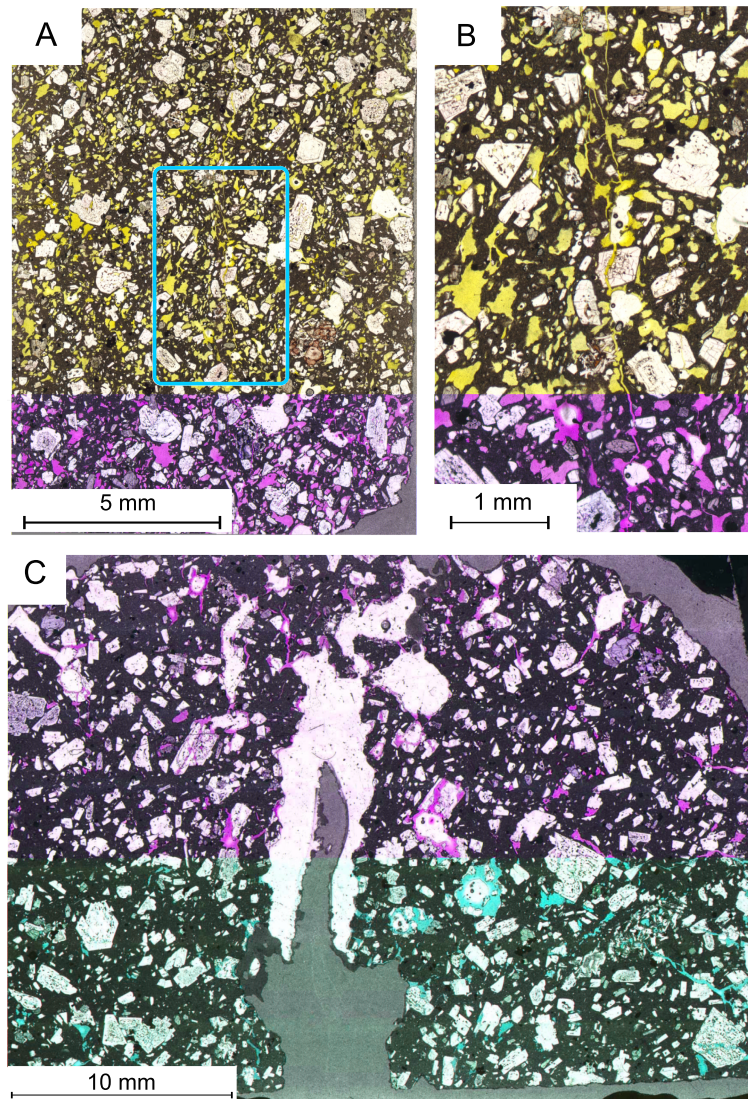
Figure 5. (a) Photomicrograph showing postexperimental sample SG10J (25% Φ, T_s of 796.4 °C and $\dot{\varepsilon}_d$ of 10^{-4} s^{-1}). Thin sections have been impregnated with fluorescent epoxy so that vesicles and fractures show as yellow. A thin, branching, occasionally conjugate fracture passes through the center of the sample. The blue box in the center of the sample is enlarged in panel (b), allowing the fracture pathway to be seen. Alignment of vesicles is minor, with long axes preferentially from top right to bottom left. (b) Cropped region with the fracture path highlighted. Note the presence of conjugate and en-echelon fractures and the tendency for fractures to deviate toward vesicles and crystals. (c) Postexperimental sample SGPF13C (3% Φ, T_s of 795.9 °C and $\dot{\varepsilon}_d$ of 10^{-4} s^{-1}) showing irregular, crenulated fracture boundaries that develop incrementally from crystal to crystal. Radial fractures can also be seen propagating inward from the right-hand boundary of the sample. Small fractures can be seen propagating above the main fracture toward the top of the sample. The contact between the sample and the pistons widened in this sample (Figure 4d) and the fracture became significantly dilated for axial compression >1 mm.

4. Discussion

4.1. Terminology and Deformation Modes

The definition and discrimination of deformation regimes and failure modes is an essential task, as the classic interpretation of mechanical data and tensile strength calculation hinges upon assumptions of elastic stress accumulation and a brittle failure mode. During high-temperature testing, sample deformation may range between fully brittle and fully ductile (or viscous), and sample failure may not be guaranteed. Therefore, we define a brittle regime as one in which elastic stress, or load, shows a stable, near-linear progression with respect to displacement until failure and where damage is localized in a single throughgoing fracture, parallel to the axis of displacement. In brittle tests, the loading rate typically increases from the
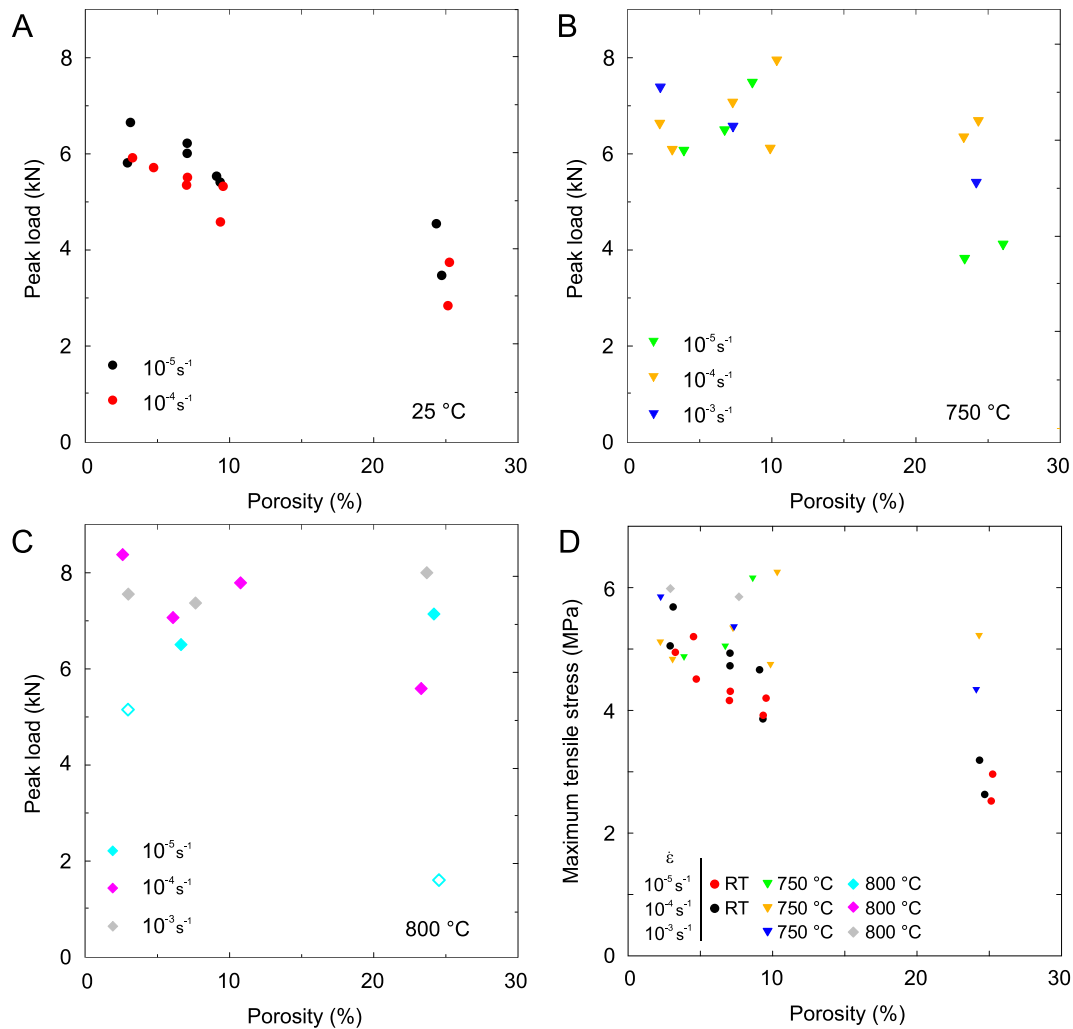
Figure 6. The load at failure during indirect tensile tests is presented against sample porosity for tests at T_s of (a) 25 °C, (b) 752.4 ± 11.3 °C, and (c) 800.8 ± 12 °C, to help distinguish trends across different testing conditions. The hollow symbols in panel (c) indicate experiments that were stopped at ≥1-mm axial compression without reaching failure. The tensile strength for tests, where valid, is plotted in (d), using the same symbols as in (a)–(c). Note that the tensile strength of dome rocks decreases with increasing porosity at room temperature and that samples with the same porosity often fail at a higher load during high-temperature tests compared to room temperature tests.

onset of loading (variably linearly or nonlinearly) during constant displacement rate tests; however, a consistent decrease in loading rate during tests is indicative of ductile deformation.

In rocks bearing silicate glass, such as fresh volcanic material, viscous flow above the glass transition temperature inhibits strain localization and encourages ductile deformation. Tests that show decreasing loading rate with increasing displacement (e.g., Figures 4a and 4b) or show deformation that is not localized in a single throughgoing fracture (e.g., Figure 4c) including radial fractures propagating into the sample, flattening or barreling, and fracture dilation (e.g., Figure 4d) cannot be considered as fully brittle, and equation (1) cannot be applied to calculate tensile stress. In such cases, the dominant deformation mode may be brittle, but we use identifiers of inelastic deformation to classify a mixed ductile-brittle or viscoelastic regime.

4.2. Brittle or Ductile? Defining the Deformation Regime

In order to assess the brittleness or ductility of high-temperature tests, we have proposed three criteria, empirically determined from the suite of experiments described here. We hope that further work will build upon and refine these criteria. In Figure 7, we note that all samples in room temperature tests failed before reaching a strain of 0.006 (left of the dashed line in Figure 7). At high temperature, samples that reached greater ε_d also failed at lower load. A threshold can be defined at $\varepsilon_d = 0.006$, above which the deformation
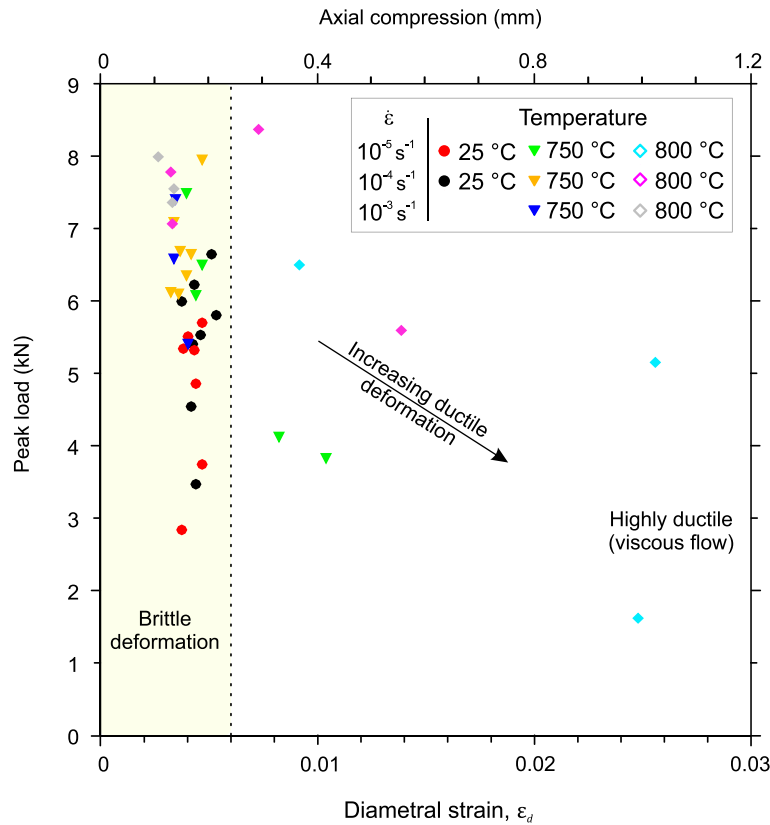
Figure 7. The peak load for every sample is plotted against the diametral strain, ε_d. Samples that underwent fully brittle behavior show a narrow range of $\varepsilon_d = 0.002 - 0.006$, compared to some materials tested at high temperature that show greater ε_d while reaching lower load (indicated by the black arrow). Two samples that did not fail within $\varepsilon_d \leq 0.025$ plot to the right of the figure, and we postulate a field for highly ductile (or viscous) deformation at such high strains, although our data are not sufficient to constrain its bounds.

mode is mixed. This is an empirical threshold that will vary when considering other materials, but a maximum ε_d threshold for brittle deformation should be constrained. Within the mixed-mode, transitional deformation field, we postulate a further threshold at high strain and low load defining a fully viscous regime, but our experimental data do not allow this to be constrained.

By examining the mechanical data, we note that the rate of loading decreases throughout tests that show $\varepsilon_d > 0.006$. We make an objective assessment of loading rate variance during all high-temperature tests by comparing the loading rate over 10 segments of the loading curve (from 10–100% of the curve prior to failure). Noise in the data was mitigated using a moving average of between 0.1% and 1% of the data points, depending on the strain rate. The loading rate was evaluated from the initiation of loading up to the point immediately before failure, as determined by a sudden drop in load. The loading rates were plotted and fit with a logarithmic regression, which provided the best fit in all but a few tests where loading rate change was smallest (see Figure 8a). The equation of the regression curves is in the form $\frac{dy}{dx} = a\ln x + b$, where a and b are constants describing the rate of change of the gradient and the vertical offset (i.e., the initial slope) respectively, and x is the normalized displacement during loading (Table 3).

We classify the nonlinearity of the loading rate using a brittleness index (BI) which we define as $BI_{m1} = \frac{a}{b}$. The lower limit for this index is -1, since load cannot fall below 0 in these tests. Negative values closer to -1 indicate more substantial decreases in loading rate prior to failure; positive values indicate increasing loading rate during tests, characteristic of brittle elastic deformation. Decreasing loading rates imply increasing strain per unit load, leading to a correlation between BI_{m1} and strain to failure (Figure 8b). In glass-bearing rocks at high temperature, the value of BI_{m1} represents the curvature of the force-displacement curve caused by the interplay between the loading rate and the relaxation of stress, but does not consider the absolute
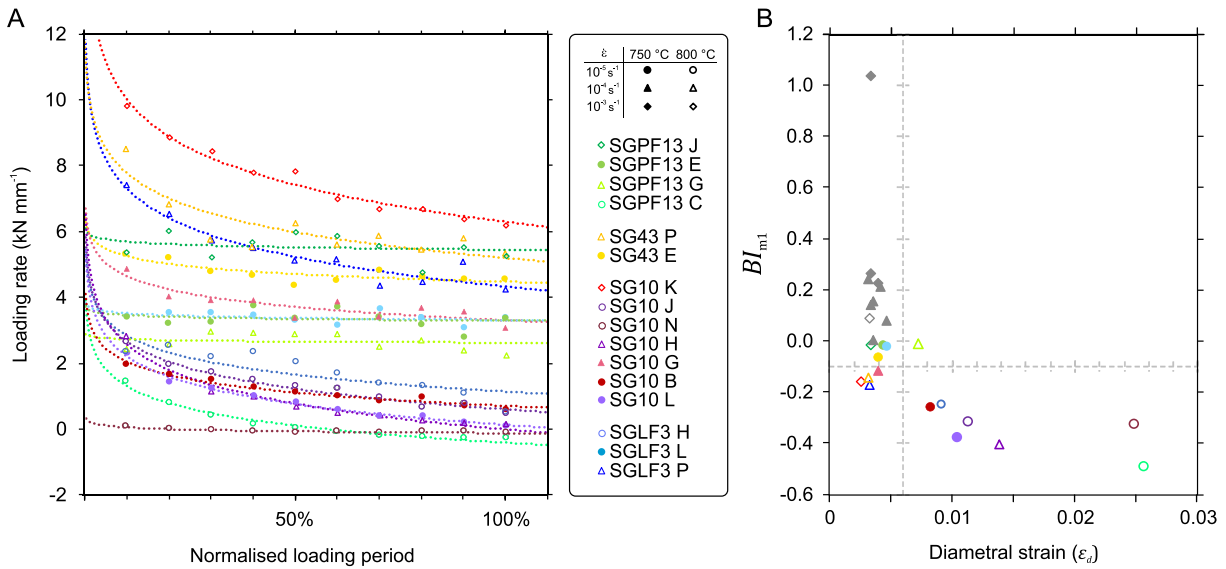
Figure 8. (a) Rate of loading plotted for 10 equal periods between 0% and 100% of prefailure loading for all high-temperature tests that showed a decrease in loading rate. Each set of points is fitted with a logarithmic regression curve in the form $\frac{dy}{dx} = a\ln x + b$, with the constants a and b given in Table 3. Symbols indicate the experimental conditions and samples. (b) Correlation between BI_{m1} and ε_d where the thresholds for fully brittle deformation are shown as gray dotted lines. Experiments in panel (a) are shown with the same symbol color, while experiments that showed positive BI_{m1} values are shown in gray.

value of the initial loading rate, b; therefore, the absolute degree of ductile or viscous deformation is not well captured. This may be better represented by an empirical formula, as it is dependent on the magnitude of the loading between experiments and the applied strain rate. For this set of experiments, the relationship $BI_{m2} = \frac{a}{b}(6 - \log b)$ where the constant in the second term will vary empirically, appears to rank the experiments more closely regarding total ductile deformation (see Table 3). Nevertheless, as the absolute degree of ductile or viscous deformation is not required to designate the deformation mode, we define a threshold using $BI_{m1} \geq -0.1$ for fully brittle deformation, which is plotted in Figure 8b.

The loading rate based brittleness indices (BI_m) we describe above can be compared to established indices from the rock mechanics and geomechanics literature. However, due to the testing method, only 2 out of 25 indices described in a recent review paper (Zhang et al., 2016) can be directly applied to our indirect tensile strength tests. We classify these two as elasticity-based indices (BI_e), as they consider the fraction of elastic strain (BI_{e1}) or elastic energy (BI_{e2}) versus the total strain or energy to failure (Hucka & Das, 1974). Since the BI_e indices are also based directly on the mechanical data, we can make a straightforward comparison against our BI_m indices. For BI_{e1}, we calculated the elastic displacement by considering the linear elastic gradient up to the peak load. The elastic gradient was taken as the b value for decreasing loading rate tests, but for increasing loading rate tests we used the average gradient between 70% and 90% of total prefailure extension (see data repository Hornby, Lavallée, Kendrick, De Angelis, et al., 2019). (Note that all tests were conducted with constant displacementrate, thus the variation in loading rate represents the differing rock responses to deformation). For BI_{e2}, the elastic energy was calculated by dividing the area under the fitted elastic force-displacement curve by the area under the measured force-displacement curve (Hucka & Das, 1974). To calculate the latter value, we fitted a second-order polynomial to the measured curve and integrated up to the point of failure. All BI values are given in Table 3, with fitting curves given in the data repository. A comparison of all four indices (Figure S1a) shows similar trends, but BI_{m2} and BI_{e2} show better data distribution compared to the other two. Only BI_m values discriminate between decreasing and increasing loading rates in the brittle regime, and only BI_{m2} identifies the very low loading rate of test SG10N. We compare BI_{m2} and BI_{e2} against strain in Figure S1b. All brittle experiments defined by the BI_{m1} criterion are well discriminated above a value of 0.8 in BI_{e2}, supporting our chosen threshold. This clear separation shows that elastic energy absorption by viscous flow may be the most sensitive indicator for small degrees of viscous deformation. Since this is an independent measure, we can add the $BI_{e2} > 0.8$ threshold to the definition for fully brittle deformation.

Table 3
Measures of Brittleness in High Temperature Experiments

Sample	T_s (°C)	T_s/T_g	Displacement rate (mm/s)	Diametral strain (ε_d)	Extension (mm)	Loading rate change (a)	Initial loading rate (b)	BI_{m1} /b	BI_{m2} a/b $(6 - \log b)$	BI_{e1}	BI_{e2}
SGLF3G	758.7	0.968	0.04	0.00343	0.136	19,485	19,974	0.976	1.658	0.773	0.912
SGPF13K	741.1	0.943	0.04	0.00344	0.137	10,254	39,202	0.262	0.368	0.868	0.926
SG43K	752.4	1.006	0.004	0.00323	0.129	8,235	35,042	0.235	0.342	0.910	0.964
SG10S	762.0	1.030	0.04	0.00406	0.162	5,635.2	25,445	0.221	0.353	0.880	0.911
SGPF13I	763.3	0.971	0.004	0.00423	0.168	6,302.9	30,568	0.206	0.312	0.886	0.931
SGPF13L	745.2	0.948	0.004	0.00362	0.144	5,280.3	34,673	0.152	0.222	0.905	0.939
SGLF3F	742.6	0.947	0.004	0.00338	0.134	6,059	44,094	*0.137*	0.186	0.920	0.974
SGLF3N	812.8	1.037	0.04	0.00332	0.132	4,321.6	50,281	0.086	0.112	0.920	0.942
SG43L	755.6	1.010	0.004	0.00473	0.188	3,389	44,484	0.076	0.103	0.921	1.000
SG10F	752.9	1.017	0.004	0.00366	0.146	35.43	47,474	*0.001*	0.001	0.953	0.977
SGPF13G	812.6	1.034	0.004	**0.00732**	0.291	−454.3	29,201	−0.016	−0.024	0.922	0.899
SGPF13J	789.2	1.004	0.04	0.00342	0.136	−1,070	58,699	−0.018	−0.022	0.945	0.857
SGLF3L	744.6	0.950	0.0004	0.00467	0.186	−897	36,997	*−0.024*	−0.035	0.946	0.921
SG43E	748.5	1.001	0.0004	*0.00399*	0.159	−3,389	52,575	*−0.064*	−0.082	0.899	0.870
SGPF13E	758.5	0.965	0.0004	0.00444	0.177	−3,573	39,154	*−0.091*	−0.128	0.957	0.908
SG10G	752.8	1.017	0.004	0.00400	0.159	−5,838	48,288	***−0.121***	−0.159	0.828	0.758
SG43P	788.8	1.055	0.004	*0.00325*	0.129	−11,325	78,078	***−0.145***	−0.161	0.772	0.722
SG10K	791.2	1.069	0.04	0.00266	0.106	−16,050	101,591	***−0.158***	−0.157	0.743	0.686
SGLF3P	792.6	1.011	0.004	0.00334	0.133	−13,004	74,995	***−0.173***	−0.195	0.709	0.654
SG10B	743.9	1.005	0.0004	**0.00828**	0.329	−4,973	20,741	***−0.240***	−0.404	0.605	0.552
SGLF3H	791.6	1.010	0.0004	**0.00916**	0.364	−7,438	30,337	***−0.245***	−0.372	0.589	0.532
SG10J	796.4	1.076	0.0004	*0.0113*	0.452	−8,991	28,359	***−0.317***	−0.491	0.558	0.444
SG10N	795.9	1.076	0.0004	*0.0248*	0.986	−772.2	2,360	***−0.327***	−0.860	0.691	0.503
SG10L	763.6	1.032	0.0004	*0.0104*	0.414	−9,095	24,005	***−0.379***	−0.614	0.385	0.272
SG10H	804.5	1.087	0.004	*0.0139*	0.552	−11,285	27,707	***−0.407***	−0.634	0.366	0.261
SGPF13C[a]	796.5	1.013	0.0004	**0.256**	4.093	−7,464[a]	15,084[a]	***−0.495***	−0.901	0.337	0.218

Note. Four brittleness indices—the curvature of the force-displacement data (BI_{m1} and BI_{m2}), the ratio between elastic strain and total strain at failure (BI_{e1}) and between the elastic energy and total energy at failure (BI_{e2})—are shown for each test. a and b are constants within logarithmic loading rate regression functions for each test. Bold italic values show tests with criteria indicating ductile and mixed-mode deformation. All criteria must be met for an experiment to be classified as brittle. Tests are sorted from lowest to highest BI_{m1} values.
[a] a and b were calculated on the portion of the load-displacement curve up to 1-mm extension.

In summary, including the textural evidence outlined in section 4.1, we use three criteria to define deformation regime. Experiments that are fully brittle must satisfy all three criteria, while varying degrees of ductile or viscous deformation can be assessed using the value of criteria (2) and (3) given below.

1. $\varepsilon_d \leq 0.006$ at failure.
2. $BI_{m1} \geq -0.1$ or $BI_{e2} > 0.8$;
3. Sample deformation must be limited to a single fracture with major axis parallel to the applied stress, passing through the center of the sample.

4.3. Recommendations for Conducting Indirect Tensile Tests Under Volcanically Relevant Conditions

The ISRM and ASTM guidelines for Brazilian disc tests (ASTM, 2004; ISRM, 1978) were not intended to be used to replicate natural volcanic deformation conditions. Nevertheless, the suggested methods and recent literature have been followed, where possible and appropriate (see Methods). The failure time for our samples ranges from 3 s to 19 min, with most samples failing in the recommended range (i.e., 15–600 s). All tests at a strain rate of 10^{-3} s^{-1} failed in <5 s, while tests at 10^{-5} s^{-1} that underwent ductile deformation often failed at periods >600 s. Loading rates range from 0.4 to 106 kN/min, with only experiments conducted at 10^{-4} s^{-1} lying in the recommended range (ASTM, 2004; ISRM, 1978). However, given the range of deformation modes and failure times encountered at high temperature, we believe that a recommendation for deformation rate or duration is not appropriate and that researchers should vary deformation rate according to material behavior and testing objectives. In order to attain fully brittle deformation, our results show that faster deformation rates and shorter failure times may be required to those given by ASTM and ISRM

guidelines. Since the tensile strength of volcanic materials over natural temperature and strain rate ranges is essential to understanding rock physics and eruptive mechanisms in volcanic settings, we have conducted indirect tensile tests at high temperature and variable strain rate. Here, we propose a set of recommendations for such tests and guidelines for determination of the deformation modes. These are based on the experimental data we have to hand, but since this represents the majority of all such experiments to date, perhaps such an attempt is warranted. We intend these as a reference point for other researchers, and the recommendations should not be perceived as prescriptive.

1. Crystallinity and porosity of experimental materials measured prior to testing.
2. Ideally, sample dimensions should conform to $D = 2L$ to reduce contact area increases.
3. Sample orientation in respect to any anisotropic fabric (either in pore space or crystal distribution) should be noted and provided for each test.
4. For glass-bearing materials such as volcanic rocks, the glass transition temperature, T_g, or the softening temperature should be measured prior to testing.
5. Heating rates ≤5 °C/min and temperature soak of ≥1 hr recommended to limit differential expansion of constituent phases and ensure thermal homogeneity.
6. Machine compliance should be measured at test temperature(s), and a nonlinear function (e.g., Gruber, 2018) should be used to correct test data.
7. Test temperature should refer to sample temperature measured in situ, and offset to furnace set point should be noted.
8. Load on the sample should be avoided (or minimized if unavoidable) during heating and prior to the start of the test to prevent pretest deformation.
9. Displacement and strain may be reported along the sample axis parallel to the applied force and referred to as axial strain or diametral strain rather than tensile strain.
10. The ductile-brittle failure criteria described in section 4.2 should be used to determine deformation mode:

i　$\varepsilon_d \leq 0.006$
ii　$BI_{m1} \geq -0.1$ or $BI_{e2} > 0.8$
iii　Sample deformation must be limited to a single fracture with major axis parallel to the applied stress, passing through the center of the sample.
11. For fully brittle deformation, tensile stress may be calculated and tensile strength reported using equation (1).
12. Where the brittle criteria are not met, the deformation structures or textures should be described and peak load rather than stress (or strength) should be given.

5. Application of the Findings to Volcanic Environments

5.1. Dome Lavas′ Tensile Strength and Deformation Mode Across the Ductile-Brittle Transition

Temperature is crucial in dictating the strength and deformation modes of lavas, as it controls the melt viscosity (and thus the relaxation rate; e.g., Dingwell & Webb, 1989) and may regulate the volume of lava (e.g., Gottsmann & Dingwell, 2000). The onset of viscoelastic relaxation is expected for glass-bearing dome rocks above the glass transition temperature, here approximated using the softening point, recorded at 740–786 °C in our samples (see Table 1). The indirect tensile disc tests carried out here demonstrate that the rheology of dome lavas is also strongly controlled by the strain rates they experience and weakly controlled by the porosity at high temperatures. We assess the dependence of the brittleness index values calculated for each test on these parameters using a composite plot (Figure 9) where T_s is normalized to the glass transition temperature. We plot T_s/T_g against BI_{m2} in Figure 9a and designate color and size to the data points to represent $\dot{\varepsilon}_d$ and sample porosity, respectively. It is immediately apparent that temperatures below T_g result in brittle deformation and failure (plotting below the gray dashed threshold), while with increasing temperature overshoot (above T_g), we observe an increasingly ductile (or viscous) component of deformation. We plot linear regressions for data points at each $\dot{\varepsilon}_d$, which are subparallel but offset to greater brittleness at higher strain rate. This simple relationship shows brittle deformation extending further above T_g for higher $\dot{\varepsilon}_d$. The linear regression may be too simplistic, especially for positive brittleness values, which are expected to plateau a little above 0, but it is feasible for deformation within the near-T_g range plotted here. In Figure 9b we plot

the data against BI_{e2}, representing the fraction of elastic energy. All fully brittle data collapse close to 1, while two trends of decreasing brittleness are distinguished, one close to T_g and one at $T_s/T_g > 1.05$. In the latter range, all tests were mixed mode to viscous dominated. These two clusters of data are a product of the differing glass transition temperatures and two furnace set point temperatures, but it is notable that similar trends are observed over both T_s/T_g ranges, suggesting a minor effect of groundmass melt viscosity on the total energy absorption; however, data are sparse for the higher T_s/T_g data. Temperature is shown to be a key control on deformation mode; thus, there is a need to better resolve the temperature conditions in our assessment of the state of magma during volcanic unrest.

Porosity is a controlling parameter on the tensile strength and deformation mode of volcanic rock—as observed in previous studies (Spieler et al., 2004; Zorn et al., 2018)—and we find that σ_t follows a linear trend with Φ at room temperature, but this dependence is lessened at temperatures relevant for dome lavas (Figures 6 and 9), especially at lower strain rates where viscous flow dominates. This observation has also been found in uniaxial compression experiments on dacitic lava (Coats et al., 2018) suggesting a temperature-dependent sensitivity of failure stress to porosity. When deformed at high temperature, samples' strength also appears to be more variable for a given porosity. We see a significant increase in ε_d at $T_s > T_g$ during deformation at low strain rates (Figures 4, 7, and 9 and Table 3), indicating a contribution of the melt's viscous response on mechanical behavior. The role of Φ in decreasing rock strength during mixed mode and viscous deformation appears to be diminished, and pores may favor a certain degree of pervasive strain and stress relaxation. We may expect a stronger porosity dependence of the tensile strength during high-temperature tests at strain rates close to and above the relaxation time of the silicate melt (e.g., above the fully brittle threshold where brittle deformation mechanics govern failure (Coats et al., 2018; Dingwell & Webb, 1989; Wadsworth et al., 2017)).

Above T_g, the strain rate determines the rheological behavior (i.e., deformation mode) of lavas. We find that an increase in strain rate lowers ε_d and results in a higher apparent tensile strength (Figure 7); an observation previously made for dome lava deformed in compression (Lavallée et al., 2013). Brittle behavior can be met at high strain rates (Figure 9a) preventing stress relaxation and strain, thus favoring the development of a localized throughgoing fracture. As temperature drops the lava also becomes increasingly brittle as the degree of strain localization increases (Coats et al., 2018; Lavallée et al., 2008). In many cases where the applied strain rate is lower, a certain degree of stress relaxation (see Figure 8) and pervasive strain (see Figures 7 and 9) results in slow tearing and the development of blunt crack tips (see Figure 5c). In such cases, the onset of deformation will lead to transient stress accumulation as the material stiffens, before partially dissipating the stress through viscous relaxation and flow, resulting in loading rate decrease from an initial maximum (Figure 8). This degree of viscous relaxation is determined by the ratio of the deformation timescale to the relaxation timescale (Dingwell & Webb, 1989; Maxwell, 1867) and equivalent relationships when considering multiphase suspensions (Coats et al., 2018; Wadsworth et al., 2018). With increasing ductility, primary fracture propagation becomes increasingly time dependent and incremental. This can be seen in the crenulated fracture path propagating between crystals and void spaces (Maire et al., 2016), and the widening of existing fractures seen in samples deformed at high temperature and low strain rate (Figures 4 and 5c).

For tests with fully brittle deformation we find on average an increase in tensile strength at high temperature (see Tables 2 and 3), for a given porosity (i.e., lavas are stronger than their corresponding cool, rock counterparts). This conforms with the recent results from basaltic lavas in direct tension (Lamur et al., 2018) and to results of low-to-high temperature compressive strength tests on basalt from Pacaya (Schaefer et al., 2015) and dacites from Mount Unzen (Coats et al., 2018). Finally, at ambient (room) temperature, the tensile strength of the tested dome rocks is mildly influenced by strain rate. An increase of 1 order of magnitude (10^{-5} vs. 10^{-4} s^{-1}) results in mild strengthening, in agreement with previous studies that demonstrated rate strengthening in compression (Coats et al., 2018; Schaefer et al., 2015). The cause of this rate strengthening has been postulated as an inability of the sample to equilibrate to its imposed stress conditions (Coats et al., 2018), resulting in a lag between the application of a critical stress and the propagation of a pervasive fracture, which we believe can explain the observations here.

5.2. Tensile Rupture at Santiaguito: A Constraint on Outgassing Versus Explosive Events

The experimental findings presented here show that the development of tensile fractures in lavas is temperature and deformation rate dependent. The outer parts of a lava dome (i.e., the carapace and talus) are prone
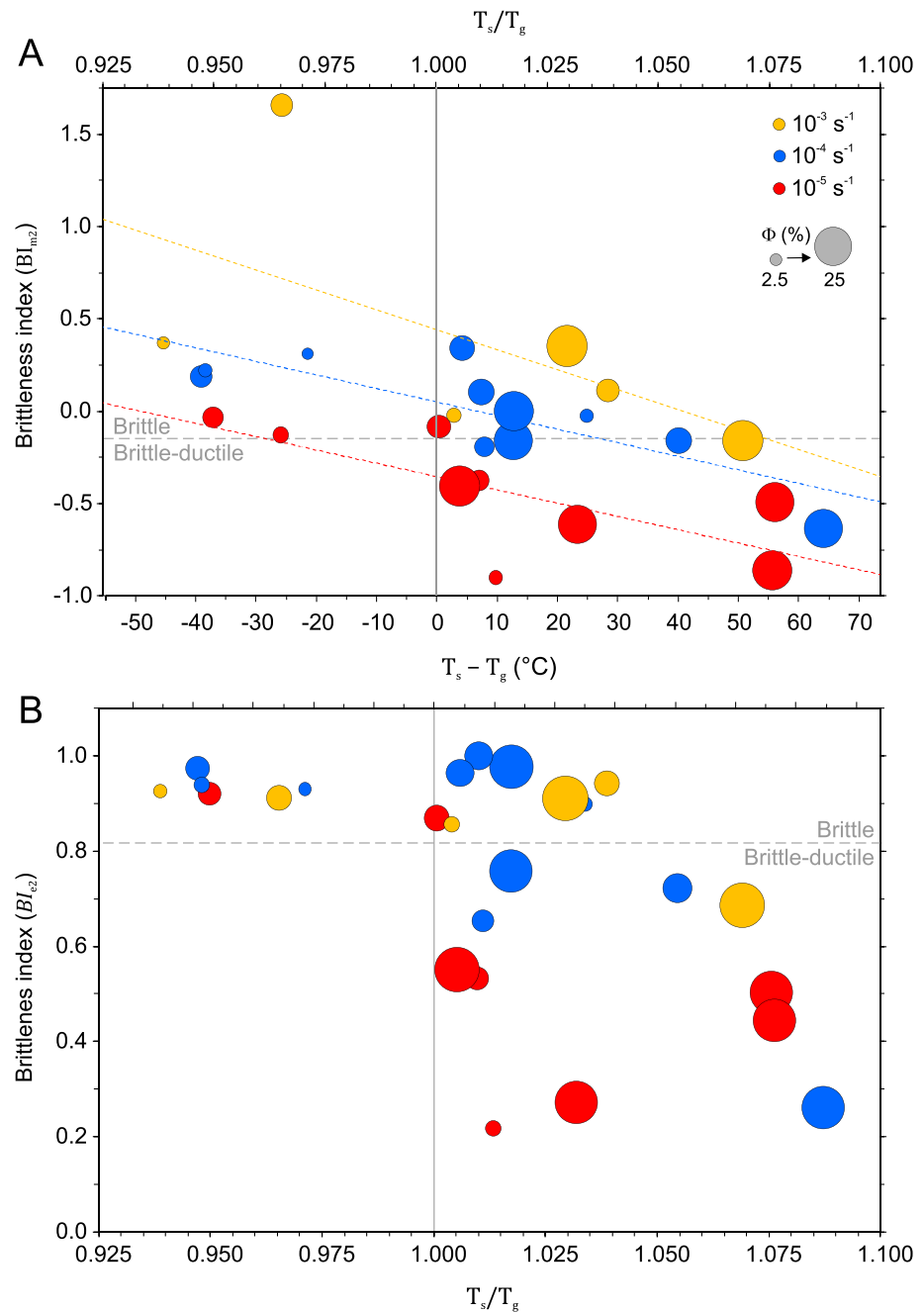
Figure 9. A composite plot showing the effects of strain rate, temperature, and porosity on the brittleness indices at high temperature. Sample temperatures are normalized to the glass transition temperature for each test, highlighting the effect of viscous flow of groundmass glass on bulk brittleness. (a) Plotting against BI_{m2} shows that for $T_s < T_g$, all tests had a brittle failure mode. When $T_s/T_g > 1$, increasing temperatures for a given strain rate lead to decreasing brittleness. Linear regressions describe subparallel trends where brittleness is inversely correlated with T_s/T_g, offset for higher brittleness with increasing strain rate. Hence, brittle failure modes extend further above T_g at higher strain rates. (b) The bounds $0 \leq BI_{e2} \leq 1$ lead to a sigmoidal decrease in brittleness as temperatures increase from T_g. Two discrete but similar trends of diminishing brittleness can be seen. The separation of the data is due to the two set point temperatures (e.g., 800 and 850 °C) and two clusters of T_g (e.g., ~745 and ~785 °C). We note that only samples deformed at 10^{-5} s^{-1} undergo substantial ductile energy absorption at T_s/T_g values close to unity. At $T_s/T_g > 1.05$, samples deformed at intermediate and high strain rates also become ductile. Porosity has a relatively minor effect on both BI values at high T_s, which we also observe in Figure 6.

to undergo cooling to the atmosphere, and as such we expect different temperatures and dominant deformation mode across the lava dome structures. If this is the case, then the stress and temperature profiles across a lava dome may favor the propagation of tensile fractures downward toward, or upward from, a pressure source.

Analysis of the cyclic tilt signals of eruptive events in 2014–2015 reveals a 5- to 6-min pressurization phase leading to outgassing or explosive events, an observation previously made during eruption monitoring in 2012 (Johnson et al., 2014; Lavallée et al., 2015). In particular, we note that tilt signals leading to outgassing events reach a lower amplitude than the tilt signals leading to explosive eruptions. As the timescale of inflation is similar in the event of outgassing (6 min) or of explosions (5 min), then we find that the sustained strain rate experienced by magma prior to explosions is greater, assuming that the tilt source location and temperature remain the same.

The control of the applied diametral strain rate on ε_d is further shown in Figure 10; this effect is accentuated with increasing temperature above T_g due to an increasing viscous contribution to deformation (Figures 10b and 10c). Within the $\dot{\varepsilon}_d$ and ε_d domains, we explore the timescales and rates of failure constrained by monitoring signals at Santiaguito (i.e., the positive tilt timescale to explosions). The total strain accumulated during the period of inflation can be approximated as a function of strain rate throughout the measured inflation period; the monitoring data show a brief nonlinear acceleration at the onset of inflation (Figure 3) before reaching constant inflation rate; however, here we use a simple model assuming that inflation rate is constant throughout the inflation minute period. We plot the total strain experienced by the lava dome if subjected to different strain rates for periods of 5 and 6 min (i.e., the red curves plotted against the secondary x axis in Figures 10a–10c) and define the region (shaded in red) where these curves intersect the upper and lower bounds of ε_d at failure, experimentally constrained for different rocks tested at eruptive temperatures (red shading). This provides a means to assess the conditions which may lead to rupture during outgassing and explosive phases at Santiaguito (Note that in our analysis we avoid any considerations of length scale dependence on rupture). Outgassing phases are preceded by 6 min of inflation; in this scenario, we anticipate that lava deformation is dominantly viscous, with tearing and time-dependent fracturing but probably no extensive fracturing which could cause deep-seated fragmentation. Thus, by comparing the aforementioned intersection of the curves in Figure 10, we estimate that over a period 6 min, the lava dome would have experienced strain rates slower than $6.5 \times 10^{-5}\,\mathrm{s}^{-1}$ to a maximum of 0.026 strain for the deeper part of the dome at $T_s/T_g > 1.05$ and strain rates slower than $3.5 \times 10^{-5}\,\mathrm{s}^{-1}$ to a maximum of 0.014 strain for the peripheral part of the dome at $1 < T_s/T_g < 1.05$ (The experimental data suggest that faster strain rates or more strain would result in complete rupture). As an upper bound, assuming that such conditions are experienced across the whole dome (~200 m wide), it would imply that the dome experienced deformation rates <8–14.5 mm/s for a maximum displacement <2.8–5.2 m. Explosive events, for which we anticipate magma rupture and fragmentation, are preceded by 5 min of inflation. From Figure 9, we estimate that the lava dome would have experienced strain rates $>7.1 \times 10^{-5}\,\mathrm{s}^{-1}$ for the hotter parts of the dome at $T_s/T_g > 1.05$ and strain rates $>4 \times 10^{-5}\,\mathrm{s}^{-1}$ for the part of the dome at 750 °C. Following the above reasoning, it would imply that the dome would have deformed at rates >8–14.2 mm/s prior to explosions. Johnson et al. (2014) used particle image velocimetry to measure up to 20 cm/min (or 3.3 mm/s) average vertical velocities of the dome surface preceding both outgassing and explosive phases. Given the continuous lateral movement of dome lava (feeding lava flows to the SE; Figure 1) noted during these measurements, this shows that our analysis compares well to their observations. This simple analysis indicates that the experimental conditions tested in this study can provide reliable first-order constraints for deformation leading to outgassing and explosive activity at Santiaguito and, together with data from Figure 9a, demonstrates that small changes in strain rate or temperature, prompted by the stalling of rising magma for instance, can lead to transitions from passive to explosive activity.

These strain rate constraints allow us to better infer the deformation modes within the conduit. Since our estimate of magmatic temperature at Santiaguito is somewhat conservative (i.e., Stoiber & Rose, 1969, measured 843 °C), we conclude that a degree of ductile and viscous deformation is inevitable during 5–6 min of continuous deformation over the strain rates given above and at a postulated pressure source depth of 300 m. In shallow volcanic systems, the damage developed through ductile deformation accompanied by the pervasive development of microfractures (those that do not coalesce to complete rupture) results in increased pore
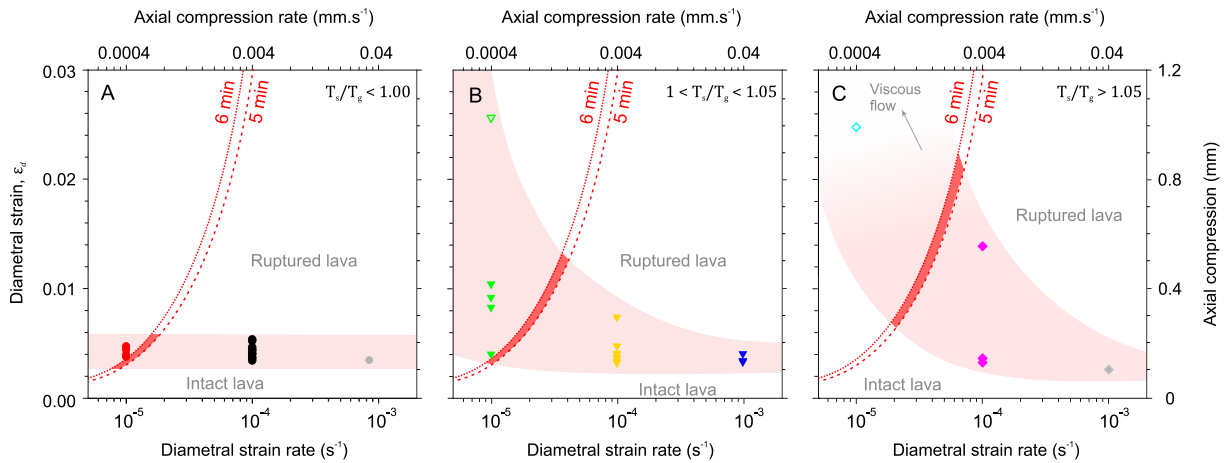
Figure 10. Diametral strain rate ($\dot{\varepsilon}_d$) plotted against strain to failure (ε_d) defines failure timescales. We plot the data in three temperature classes: below T_g (a), just above T_g (b), and above T_g (c), as defined by T_s/T_g ranges given in the top-right of each panel. Below T_g, all tests fail within a narrow range of ε_d (0.0025–0.006), while above T_g, we observe an increase in ε_d with a decrease in $\dot{\varepsilon}_d$. We bracket the experimental results at each temperature (pink field) and highlight in red where this field intersects 5- and 6-min constant deformation trajectories (shown as red dotted and dashed lines). The red fields constrain the strain and strain rate conditions for failure of magma or lava within the monitored inflation timescales prior to explosions and outgassing, respectively, at Santiaguito. Close to T_g, brittle or mixed-mode deformation at $10^{-5} < \dot{\varepsilon}_d < 4\times10^{-5}$ s^{-1} leads to failure, while at $T_s/T_g > 1.05$ failure can be achieved at $2\times10^{-5} < \dot{\varepsilon}_d < 8\times10^{-5}$ s^{-1}, with substantially greater strain accumulation. Under low $\dot{\varepsilon}_d$ and high ε_d the dominant deformation mode becomes viscous flow, as indicated by the arrow in panel (c).

space, affecting gas accumulation and release, as well as buoyancy, and thus regulating the stress balance responsible for the monitored activity and signals (e.g., Edmonds et al., 2003). Local dilatancy could increase shear stress and weaken magma at conduit margins that may trigger shear failure, fault slip, and thermal vesiculation, leading to explosive events; however, pervasive deformation would also increase the connectivity of the porous pathways and the permeability of the lava volume (Kendrick et al., 2013; Lamur et al., 2017; Lavallée et al., 2013), enabling more efficient outgassing to occur (Edmonds et al., 2003; Eichelberger et al., 1986; Mueller et al., 2008) and potentially alleviating the pressure that drives explosions (Okumura et al., 2009). Thus, small variations in the volatile flux and the state of permeability in the upper lava dome may lead to transitions between explosive eruption or passive degassing during inflation and resulting ductile-brittle deformation. This may provide an explanation for regular gas emission events and ash-poor explosions at Santiaguito. Repeated episodes of ductile-brittle damage may be an essential element in maintaining a system perched at the explosive-passive threshold and generating the long-term nondestructive eruption dynamic at Santiaguito.

The surficial, outer carapace of the lava dome resides at lower temperatures, close to or below the glass transition of the lava (Sahetapy-Engel & Harris, 2009), and our work suggests that it would experience dominantly brittle deformation, except at the lowest strain rates (see Figure 10b). Therefore, we anticipate that ruptures initiate at the surface and propagate downward into the lava core. This may (1) expose the pressurized regions of the lava dome, which may encourage degassing and outgassing if permeability is high due to ductile deformation and slow tearing at low strain rate or (2) favor magmatic fragmentation if rupture is brittle and rapid, and deformation is too localized to permit passive gas release. The fluctuation between passive outgassing and explosive activity at Santiaguito may be triggered by small variations in ductility and crack propagation (slow versus rapid rupture) downward from the dome carapace at Caliente. The importance of the degree of ductile deformation in maintaining a mild, nondestructive eruption style and determining the style of activity indicates that the long-term stability of the system may be highly sensitive to changes in the temperature, composition, and volatile content of magma.

6. Conclusion

Visual and geophysical observations combined with indirect tensile strength tests are used to describe the rheology and deformation mode of dome lava and the consequences for the eruptive behavior of the Caliente dome at Santiaguito. We observe that the eruption exhibits continuous outgassing during interexplosion periods and that inflationary tilt signals precede (i) gas-and-ash explosions that leave the dome structure intact or (ii) gas-rich plumes. The monitoring signals show regular 5- to 6-min inflation signals

preceding these volcanic emissions; however, the rate and magnitude of inflation are greater prior to gas-and-ash explosions, suggesting that higher strain rates are experienced by the lava dome. We deduce that failure by bulk overpressure of a bubbly magma cannot generate the observed explosive activity localized around faults and requires the development of tensile fractures.

We used the indirect tensile strength testing method at low and high temperature and constrained the mechanical behavior of Santiaguito dome lavas in tension to simulate shallow deformation cycles at Santiaguito. In order to classify deformation modes across the brittle-ductile transition, we use BIs, including two novel indices based on the loading rate change during tests, as well as an established BI based on energy partitioning. We establish threshold values for the BIs and total strain to failure to constrain fully brittle and mixed-mode (brittle-ductile) deformation. In the brittle regime, the tensile strength of dome lavas is inversely proportional to porosity and is lower at ambient as opposed to magmatic temperatures. At eruptive temperatures above the glass transition temperature of the lava, we find that fully brittle deformation dominates only at higher strain rates. We observe an increasing degree of ductile deformation at higher temperatures and lower strain rate, which manifests as an increase in the strain accumulated prior to failure (which is partitioned between slow tearing and viscous relaxation of lava) and a decreasing loading rate during the tests. We develop BIs to evaluate deformation mode based on the loading rate and provide a set of recommendations for conducting high-temperature indirect tensile strength tests and interpreting the results of mixed-mode deformation. We find an empirical threshold for fully brittle failure of <0.006 strain and a trend for decreasing strength when strain exceeds 0.006. At high temperature and low strain rate sample strength shows only minor porosity dependence and pores may favor an increased degree of ductility. Comparison with timescales of monitored inflation at Santiaguito shows that mixed ductile-brittle deformation is inevitable during inflation at the modeled depth range, while brittle deformation is more likely to occur in the outer portions of the dome and in the dome carapace where temperatures approach or fall below the glass transition. Ductile deformation leads to increased dilatancy and distributed damage, which may enhance the lava permeability leading to more efficient outgassing. Repeated episodes of ductile-brittle deformation may help to maintain the low-magnitude, nondestructive eruption style at Santiaguito. Lower temperatures at the dome surface are more likely to result in localized brittle failure of lava, which may expose pressurized areas of the lava dome and trigger explosive eruptions. In an eruptive scenario, rapid outgassing would oppose and reduce the normal stress applied on the faults, making them more likely to shear and trigger thermal vesiculation, both contributing to the likelihood of fragmentation and explosive eruption. Our findings show that small variations in fracture geometry and permeability can determine eruptive style, and ductile damage may be a common factor in maintaining long-term eruptive activity at lava dome volcanoes. Our results highlight that strain is a key measure to determine deformation mode in high-temperature rock strength tests and demonstrate the need to better constrain the temperature and strain rate profile in shallow magma as the rate of stress accumulation dictates fracture dynamics and eruptive style.

Samples and Data

Excel data files for each experiment are openly available (CC BY 4.0) and hosted on the Open Science Framework (https://doi.org/10.17605/OSF.IO/35REB; Hornby, Lavallée, Kendrick, De Angelis, et al., 2019). All other data used in this study are included in the figures and tables within the manuscript.

References

Albino, F., Pinel, V., Massol, H., & Collombet, M. (2011). Conditions for detection of ground deformation induced by conduit flow and evolution. *Journal of Geophysical Research*, *116*, B06201. https://doi.org/10.1029/2010JB007871

Alidibirov, M., & Dingwell, D. B. (1996). Magma fragmentation by rapid decompression. *Nature*, *380*(6570), 146–148. https://doi.org/10.1038/380146a0

ASTM. (2004). Standard test method for splitting tensile strength of intact rock core specimens. Annual Book of ASTM Standards.

Balme, M. R., Rocchi, V., Jones, C., Sammonds, P. R., Meredith, P. G., & Boon, S. (2004). Fracture toughness measurements on igneous rocks using a high-pressure, high-temperature rock fracture mechanics cell. *Journal of Volcanology and Geothermal Research*, *132*(2-3), 159–172. https://doi.org/10.1016/S0377-0273(03)00343-3

Bean, C. J., de Barros, L., Lokmer, I., Métaxian, J. P., O'Brien, G., & Murphy, S. (2014). Long-period seismicity in the shallow volcanic edifice formed from slow-rupture earthquakes. *Nature*, *7*(January), 71–75. https://doi.org/10.1038/ngeo2027

Benson, P. M., Heap, M. J., Lavallée, Y., Flaws, A., Hess, K. U., Selvadurai, A. P. S., et al. (2012). Laboratory simulations of tensile fracture development in a volcanic conduit via cyclic magma pressurisation. *Earth and Planetary Science Letters*, *349-350*, 231–239. https://doi.org/10.1016/j.epsl.2012.07.003

Bluth, G. J. S., & Rose, W. I. (2004). Observations of eruptive activity at Santiaguito volcano, Guatemala. *Journal of Volcanology and Geothermal Research*, *136*(3–4), 297–302. https://doi.org/10.1016/j.jvolgeores.2004.06.001

Cassidy, M., Cole, P. D., Hicks, K. E., Varley, N. R., Peters, N., & Lerner, A. H. (2015). Rapid and slow: Varying magma ascent rates as a mechanism for Vulcanian explosions. *Earth and Planetary Science Letters*, *420*, 73–84. https://doi.org/10.1016/j.epsl.2015.03.025

Chouet, B. (1988). Resonance of a fluid-driven crack: Radiation properties and implications for the source of long-period events and harmonic tremor. *Journal of Geophysical Research*, *93*(B5), 4375–4400. https://doi.org/10.1029/JB093iB05p04375

Chouet, B., Dawson, P. B., & Arciniega-Ceballos, A. (2005). Source mechanism of Vulcanian degassing at Popocatépetl Volcano, Mexico, determined from waveform inversions of very long period signals. *Journal of Geophysical Research*, *110*, B07301. https://doi.org/10.1029/2004JB003524

Chouet, B., & Matoza, R. S. (2013). A multi-decadal view of seismic methods for detecting precursors of magma movement and eruption. *Journal of Volcanology and Geothermal Research*, *252*, 108–175. https://doi.org/10.1016/j.jvolgeores.2012.11.013

Coats, R., Kendrick, J. E., Wallace, P. A., Miwa, T., Hornby, A. J., Ashworth, J. D., et al. (2018). Failure criteria for porous dome rocks and lavas: A study of Mt. Unzen, Japan. *Solid Earth*, *9*(6), 1299–1328. https://doi.org/10.5194/se-9-1299-2018

De Angelis, S., & Bodin, P. (2012). Watching the wind: Seismic data contamination at long periods due to atmospheric pressure-field-induced tilting. *Bulletin of the Seismological Society of America*, *102*(3), 1255–1265. https://doi.org/10.1785/0120110186

De Angelis, S., & Henton, S. M. (2011). On the feasibility of magma fracture within volcanic conduits: Constraints from earthquake data and empirical modelling of magma viscosity. *Geophysical Research Letters*, *38*, L19310. https://doi.org/10.1029/2011GL049297

De Angelis, S., Lamb, O. D., Lamur, A., Hornby, A. J., von Aulock, F. W., Chigna, G., et al. (2016). Characterization of moderate ash-and-gas explosions at Santiaguito volcano, Guatemala, from infrasound waveform inversion and thermal infrared measurements. *Geophysical Research Letters*, *43*, 6220–6227. https://doi.org/10.1002/2016GL069098

Dingwell, D. B. (1996, August 23). Volcanic dilemma—Flow or blow? *Science*, *273*(5278), 1054–1055. https://doi.org/10.1126/science.273.5278.1054

Dingwell, D. B., & Webb, S. L. (1989). Structural relaxation in silicate melts and non-Newtonian melt rheology in geologic processes. *Physics and Chemistry of Minerals*, *16*(5), 508–516. https://doi.org/10.1007/BF00197020

Edmonds, M., Oppenheimer, C., Pyle, D. M., Herd, R. A., & Thompson, G. (2003). SO2 emissions from Soufrière Hills Volcano and their relationship to conduit permeability, hydrothermal interaction and degassing regime. *Journal of Volcanology and Geothermal Research*, *124*(1–2), 23–43. https://doi.org/10.1016/S0377-0273(03)00041-6

Eggertsson, G. H., Lavallée, Y., Kendrick, J. E., & Markússon, S. H. (2018). Improving fluid flow in geothermal reservoirs by thermal and mechanical stimulation: The case of Krafla volcano, Iceland. *Journal of Volcanology and Geothermal Research*. https://doi.org/10.1016/j.jvolgeores.2018.04.008

Eichelberger, J. C., Carrigan, C. R., Westrich, H. R., & Price, R. H. (1986). Non-explosive silicic volcanism. *Nature*, *323*(6089), 598–602. https://doi.org/10.1038/323598a0

Eiler, J., Carr, M. J., Feigenson, M. D., Patino, L. C., & Walker, J. a. (2003). Volcanism and geochemistry in Central America: Progress and problems. *Inside the Subduction Factory, Geophysical Monograph Series*, *138*, 153–174. https://doi.org/10.1029/138GM09

Escobar-Wolf, R. (2010). Santiaguito dome geologic map 2006 domes and lava flows. *Geological Society of America Digital Map and Chart Series*. https://doi.org/10.1130/2010.DMCH008

Esse, B., Burton, M., Varnam, M., Kazahaya, R., Wallace, P. A., von Aulock, F., et al. (2018). Quantification of ash sedimentation dynamics through depolarisation imaging with AshCam. *Scientific Reports*, *8*(1), 15680. https://doi.org/10.1038/s41598-018-34110-6

Gardner, J. E., Wadsworth, F. B., Llewellin, E. W., Watkins, J. M., & Coumans, J. P. (2018). Experimental sintering of ash at conduit conditions and implications for the longevity of tuffisites. *Bulletin of Volcanology*, *80*(3). https://doi.org/10.1007/s00445-018-1202-8

Gong, F., Zhang, L., & Wang, S. (2019). Loading rate effect of rock material with the direct tensile and three Brazilian disc tests. *Advances in Civil Engineering*, *2019*, 1–8. https://doi.org/10.1155/2019/6260351

Gottsmann, J., & Dingwell, D. B. (2000). Supercooled diopside melt: Confirmation of temperature-dependent expansivity using container-based dilatometry. *Contributions to Mineralogy and Petrology*, *139*(2), 127–135. https://doi.org/10.1007/PL00007666

Gruber, J. A. (2018). Accurate data reduction for the uniaxial compression test. *Experimental Techniques*, *42*(2), 209–221. https://doi.org/10.1007/s40799-017-0215-0

Hall, M. L., Steele, A. L., Bernard, B., Mothes, P. A., Vallejo, S. X., Douillet, G. A., et al. (2015). Sequential plug formation, desintegration by vulcanian explosions, and the generation of granular pyroclastic density currents at Tungurahua Volcano (2013-2014), Ecuador. *Journal of Volcanology and Geothermal Research*, *306*, 90–103. https://doi.org/10.1016/j.jvolgeores.2015.09.009

Harnett, C. E., Kendrick, J. E., Lamur, A., Thomas, M. E., Stinton, A., Wallace, P. A., et al. (2019). Evolution of mechanical properties of lava dome rocks across the 1995–2010 eruption of Soufrière Hills Volcano, Montserrat. *Frontiers in Earth Science*, *7*(February), 1–18. https://doi.org/10.3389/feart.2019.00007

Harris, A., Rose, W., & Flynn, L. (2003). Temporal trends in lava dome extrusion at Santiaguito 1922–2000. *Bulletin of Volcanology*, *65*(2), 77–89. https://doi.org/10.1007/s00445-002-0243-0

Heap, M. J., Farquharson, J. I., Baud, P., Lavallée, Y., & Reuschlé, T. (2015). Fracture and compaction of andesite in a volcanic edifice. *Bulletin of Volcanology*, *77*(6), 55. https://doi.org/10.1007/s00445-015-0938-7

Holland, A. S. P., Watson, I. M., Phillips, J. C., Caricchi, L., & Dalton, M. P. (2011). Degassing processes during lava dome growth: Insights from Santiaguito lava dome, Guatemala. *Journal of Volcanology and Geothermal Research*, *202*(1–2), 153–166. https://doi.org/10.1016/j.jvolgeores.2011.02.004

Hornby, A. J., Kendrick, J. E., Lamb, O. D., Hirose, T., De Angelis, S., von Aulock, F. W., et al. (2015). Spine growth and seismogenic faulting at Mt. Unzen, Japan. *Journal of Geophysical Research: Solid Earth*, *120*, 4034–4054. https://doi.org/10.1002/2014JB011660

Hornby, A. J., Lavallée, Y., Kendrick, J. E., De Angelis, S., Lamur, A., Lamb, O. D., et al. (2019). Brittle-ductile deformation and tensile rupture of dome lava during inflation at Santiaguito, Guatemala - Data. *Open Science Framework*. https://doi.org/10.17605/OSF.IO/35REB

Hornby, A. J., Lavallée, Y., Kendrick, J. E., Rollinson, G., Butcher, A. R., Clesham, S., et al. (2019). Phase partitioning during fragmentation revealed by QEMSCAN Particle Mineralogical Analysis of volcanic ash. *Scientific Reports*, *9*(1), 126. https://doi.org/10.1038/s41598-018-36857-4

Hucka, V., & Das, B. (1974). Brittleness determination of rocks by different methods. *International Journal of Rock Mechanics and Mining Sciences & Geomechanics Abstracts*, *11*(10), 389–392. https://doi.org/10.1016/0148-9062(74)91109-7

ISRM (1978). Suggested methods for determining tensile strength of rock materials. *International Journal of Rock Mechanics and Mining Sciences & Geomechanics Abstracts*, *15*(3), 99–103. https://doi.org/10.1016/0148-9062(78)90003-7

Johnson, J. B., Lees, J. M., Gerst, A., Sahagian, D., & Varley, N. (2008). Long-period earthquakes and co-eruptive dome inflation seen with particle image velocimetry. *Nature*, *456*(7220), 377–381. https://doi.org/10.1038/nature07429

Johnson, J. B., Lyons, J. J., Andrews, B. J., & Lees, J. M. (2014). Explosive dome eruptions modulated by periodic gas-driven inflation. *Geophysical Research Letters*, *41*, 6689–6697. https://doi.org/10.1002/2014GL061310

Johnson, J. B., Sanderson, R., Lyons, J., Escobar-Wolf, R., Waite, G., & Lees, J. M. (2009). Dissection of a composite volcanic earthquake at Santiaguito, Guatemala. *Geophysical Research Letters*, *36*, L16308. https://doi.org/10.1029/2009GL039370

Kendrick, J. E., Lavallée, Y., Hess, K., Heap, M. J., Gaunt, H. E., Meredith, P. G., & Dingwell, D. B. (2013). Tracking the permeable porous network during strain-dependent magmatic flow. *Journal of Volcanology and Geothermal Research*, *260*, 117–126. https://doi.org/10.1016/j.jvolgeores.2013.05.012

Kendrick, J. E., Lavallée, Y., Hirose, T., Di Toro, G., Hornby, A. J., De Angelis, S., & Dingwell, D. B. (2014). Volcanic drumbeat seismicity caused by stick-slip motion and magmatic frictional melting. *Nature Geoscience*, *7*(June), 438–442. https://doi.org/10.1038/ngeo2146

Kendrick, J. E., Lavallée, Y., Varley, N. R., Wadsworth, F. B., Lamb, O. D., & Vasseur, J. (2016). Blowing off steam: Tuffisite formation as a regulator for lava dome eruptions. *Frontiers in Earth Science*, *4*(41), 1–15. https://doi.org/10.3389/feart.2016.00041

Kilburn, C. R. J. (2003). Multiscale fracturing as a key to forecasting volcanic eruptions. *Journal of Volcanology and Geothermal Research*, *125*(3–4), 271–289. https://doi.org/10.1016/S0377-0273(03)00117-3

Lamb, O. D., De Angelis, S., Wall, R. J., Lamur, A., Varley, N. R., Reyes-Dávila, G., et al. (2017). Seismic and experimental insights into eruption precursors at Volcán de Colima. *Geophysical Research Letters*, *44*, 6092–6100. https://doi.org/10.1002/2017GL073350

Lamb, O. D., Lamur, A., Díaz-Moreno, A., de Angelis, S., Hornby, A. J., von Aulock, F. W., et al. (2019). Disruption of long-term effusive-explosive activity at Santiaguito, Guatemala. *Frontiers in Earth Science*, *6*(February), 1–14. https://doi.org/10.3389/feart.2018.00253

Lamur, A., Kendrick, J. E., Eggertsson, G. H., Wall, R. J., Ashworth, J. D., & Lavallée, Y. (2017). The permeability of fractured rocks in pressurised volcanic and geothermal systems. *Scientific Reports*, *7*(1), 6173. https://doi.org/10.1038/s41598-017-05460-4

Lamur, A., Kendrick, J. E., Wadsworth, F. B., & Lavallée, Y. (2019). Fracture healing and strength recovery in magmatic liquids. *Geology*, *47*(3), 195–198. https://doi.org/10.1130/G45512.1

Lamur, A., Lavallée, Y., Iddon, F. E., Hornby, A. J., Kendrick, J. E., von Aulock, F. W., & Wadsworth, F. B. (2018). Disclosing the temperature of columnar jointing in lavas. *Nature Communications*, *9*(1), 1432. https://doi.org/10.1038/s41467-018-03842-4

Lavallée, Y., Benson, P. M., Heap, M. J., Flaws, A., Hess, K.-U., & Dingwell, D. B. (2012). Volcanic conduit failure as a trigger to magma fragmentation. *Bulletin of Volcanology*, *74*(1), 11–13. https://doi.org/10.1007/s00445-011-0544-2

Lavallée, Y., Benson, P. M., Heap, M. J., Hess, K.-U., Flaws, A., Schillinger, B., et al. (2013). Reconstructing magma failure and the degassing network of dome-building eruptions. *Geology*, *41*(4), 515–518. https://doi.org/10.1130/G33948.1

Lavallée, Y., Dingwell, D. B., Johnson, J. B., Cimarelli, C., Hornby, A. J., Kendrick, J. E., et al. (2015). Thermal vesiculation during volcanic eruptions. *Nature*, *528*(7583), 544–547. https://doi.org/10.1038/nature16153

Lavallée, Y., Hess, K.-U., Cordonnier, B., & Dingwell, D. B. (2007). Non-Newtonian rheological law for highly crystalline dome lavas. *Geology*, *35*(9), 843. https://doi.org/10.1130/G23594A.1

Lavallée, Y., Meredith, P. G., Dingwell, D. B., Hess, K.-U., Wassermann, J., Cordonnier, B., et al. (2008). Seismogenic lavas and explosive eruption forecasting. *Nature*, *453*(7194), 507–510. https://doi.org/10.1038/nature06980

Lavallée, Y., Mitchell, T. M., Heap, M. J., Vasseur, J., Hess, K.-U., Hirose, T., & Dingwell, D. B. (2012). Experimental generation of volcanic pseudotachylytes: Constraining rheology. *Journal of Structural Geology*, *38*, 222–233. https://doi.org/10.1016/j.jsg.2012.02.001

Lensky, N. G., Sparks, R. S. J., Navon, O., & Lyakhovsky, V. (2008). Cyclic activity at Soufrière Hills Volcano, Montserrat: Degassing-induced pressurization and stick-slip extrusion. *Geological Society, London, Special Publications*, *307*(1), 169–188. https://doi.org/10.1144/SP307.10

Li, D., & Wong, L. N. Y. (2013). The Brazilian disc test for rock mechanics applications: Review and new insights. *Rock Mechanics and Rock Engineering*, *46*(2), 269–287. https://doi.org/10.1007/s00603-012-0257-7

Lin, H., Xiong, W., & Yan, Q. (2016). Three-dimensional effect of tensile strength in the standard brazilian test considering contact length. *Geotechnical Testing Journal*, *39*(1). https://doi.org/10.1520/GTJ20140268

Lyons, J. J., Waite, G. P., Ichihara, M., & Lees, J. M. (2012). Tilt prior to explosions and the effect of topography on ultra-long-period seismic records at Fuego volcano, Guatemala. *Geophysical Research Letters*, *39*, L08305. https://doi.org/10.1029/2012GL051184

Maire, E., Le Bourlot, C., Adrien, J., Mortensen, A., & Mokso, R. (2016). 20 Hz X-ray tomography during an in situ tensile test. *International Journal of Fracture.*, *200*(1-2), 3–12. https://doi.org/10.1007/s10704-016-0077-y

Markides, C. F., & Kourkoulis, S. K. (2016). The influence of jaw's curvature on the results of the Brazilian disc test. *Journal of Rock Mechanics and Geotechnical Engineering*, *8*(2), 127–146. https://doi.org/10.1016/j.jrmge.2015.09.008

Massol, H., & Jaupart, C. (2009). Dynamics of magma flow near the vent: Implications for dome eruptions. *Earth and Planetary Science Letters*, *279*(3–4), 185–196. https://doi.org/10.1016/j.epsl.2008.12.041

Matoza, R. S., Chouet, B. A., Dawson, P. B., Shearer, P. M., Haney, M. M., Waite, G. P., et al. (2015). Source mechanism of small long-period events at Mount St. Helens in July 2005 using template matching, phase-weighted stacking, and full-waveform inversion. *Journal of Geophysical Research: Solid Earth*, *120*, 6351–6364. https://doi.org/10.1002/2015JB012279

Maxwell, J. C. (1867). On the dynamical theory of gases. *Philosophical Transactions of the Royal Society of London A: Mathematical, Physical and Engineering Sciences*, *157*(January), 49–88. https://doi.org/10.1098/rstl.1867.0004

Michaut, C., Ricard, Y., Bercovici, D., & Sparks, R. S. J. (2013). Eruption cyclicity at silicic volcanoes potentially caused by magmatic gas waves. *Nature Geoscience*, *6*(10), 856–860. https://doi.org/10.1038/ngeo1928

Mueller, S., Scheu, B., Spieler, O., & Dingwell, D. B. (2008). Permeability control on magma fragmentation. *Geology*, *36*(5), 399–402. https://doi.org/10.1130/G24605A.1

Neuberg, J. W., Collinson, A. S. D., Mothes, P. A. C., Ruiz, M., & Aguaiza, S. (2018). Understanding cyclic seismicity and ground deformation patterns at volcanoes: Intriguing lessons from Tungurahua volcano, Ecuador. *Earth and Planetary Science Letters*, *482*, 193–200. https://doi.org/10.1016/j.epsl.2017.10.050

Neuberg, J. W., Tuffen, H., Collier, L., Green, D., Powell, T., & Dingwell, D. B. (2006). The trigger mechanism of low-frequency earthquakes on Montserrat. *Journal of Volcanology and Geothermal Research*, *153*(1–2), 37–50. https://doi.org/10.1016/j.jvolgeores.2005.08.008

Newman, D. A., & Bennett, D. G. (1990). The effect of specimen size and stress rate for the Brazilian test-A statistical analysis. *Rock Mechanics and Rock Engineering*, *23*(2), 123–134. https://doi.org/10.1007/BF01020397

Nishimura, T., Iguchi, M., Kawaguchi, R., Surono, H. M., & Rosadi, U. (2012). Inflations prior to Vulcanian eruptions and gas bursts detected by tilt observations at Semeru Volcano, Indonesia. *Bulletin of Volcanology*, *74*(4), 903–911. https://doi.org/10.1007/s00445-012-0579-z

Okumura, S., Nakamura, M., Takeuchi, S., Tsuchiyama, A., Nakano, T., & Uesugi, K. (2009). Magma deformation may induce non-explosive volcanism via degassing through bubble networks. *Earth and Planetary Science Letters*, *281*(3–4), 267–274. https://doi.org/10.1016/j.epsl.2009.02.036

Okumura, S., & Sasaki, O. (2014). Permeability reduction of fractured rhyolite in volcanic conduits and its control on eruption cyclicity. *Geology*, *42*(10), 843–846. https://doi.org/10.1130/G35855.1

Papale, P. (1999). Strain-induced magma fragmentation in explosive eruptions. *Nature*, *397*(6718), 425–428. Retrieved from. http://www.nature.com/nature/journal/v397/n6718/abs/397425a0.html, https://doi.org/10.1038/17109

Parisio, F., Vinciguerra, S., Kolditz, O., & Nagel, T. (2019). The brittle-ductile transition in active volcanoes. *Scientific Reports*, *9*(1), 1–10. https://doi.org/10.1038/s41598-018-36505-x

Paterson, M. S., & Wong, T.-F. (2005). Experimental rock deformation—The brittle field. In M. S. Paterson & T.-F. Wong (Eds.), *Experimental rock deformation—The brittle field* (2nd ed., Chapter 3, pp. 17–21). New York: Springer Berlin Heidelberg. https://doi.org/10.1007/b137431

Patrick, M. (2007). The gas content and buoyancy of strombolian ash plumes. *Journal of Volcanology and Geothermal Research*, *166*(1), 1–6. https://doi.org/10.1016/j.jvolgeores.2007.06.001

Perras, M. A., & Diederichs, M. S. (2014). A review of the tensile strength of rock: Concepts and testing. *Geotechnical and Geological Engineering*, *32*(2), 525–546. https://doi.org/10.1007/s10706-014-9732-0

Rhodes, E., Kennedy, B. M., Lavallée, Y., Hornby, A. J., Edwards, M., & Chigna, G. (2018). Textural insights into the evolving lava dome cycles at santiaguito lava dome, Guatemala. *Frontiers in Earth Science*, *6*(April), 30. https://doi.org/10.3389/feart.2018.00030

Rocchi, V., Sammonds, P. R., & Kilburn, C. R. J. (2003). Flow and fracture maps for basaltic rock deformation at high temperatures. *Journal of Volcanology and Geothermal Research*, *120*(1–2), 25–42. https://doi.org/10.1016/S0377-0273(02)00343-8

Rodríguez, L. A., Watson, I. M., Rose, W. I., Branan, Y. K., Bluth, G. J. S., Chigna, G., et al. (2004). SO_2 emissions to the atmosphere from active volcanoes in Guatemala and El Salvador, 1999-2002. *Journal of Volcanology and Geothermal Research*, *138*(3-4), 325–344. https://doi.org/10.1016/j.jvolgeores.2004.07.008

Rose, W. I., Chuan, R. L., Cadle, R. D., & Woods, D. C. (1980). Small particles in volcanic eruption clouds. *American Journal of Science.*, *280*(8), 671–696. https://doi.org/10.2475/ajs.280.8.671

Sahetapy-Engel, S. T., & Harris, A. J. L. (2009). Thermal structure and heat loss at the summit crater of an active lava dome. *Bulletin of Volcanology*, *71*(1), 15–28. https://doi.org/10.1007/s00445-008-0204-3

Sahetapy-Engel, S. T., Harris, A. J. L., & Marchetti, E. (2008). Thermal, seismic and infrasound observations of persistent explosive activity and conduit dynamics at Santiaguito lava dome, Guatemala. *Journal of Volcanology and Geothermal Research*, *173*(1–2), 1–14. https://doi.org/10.1016/j.jvolgeores.2007.11.026

Sanderson, R. W., Johnson, J. B., & Lees, J. M. (2010). Ultra-long period seismic signals and cyclic deflation coincident with eruptions at Santiaguito volcano, Guatemala. *Journal of Volcanology and Geothermal Research*, *198*(1–2), 35–44. https://doi.org/10.1016/j.jvolgeores.2010.08.007

Schaefer, L. N., Kendrick, J. E., Oommen, T., Lavallée, Y., & Chigna, G. (2015). Geomechanical rock properties of a basaltic volcano. *Frontiers in Earth Science*, *3*(June), 1–15. https://doi.org/10.3389/feart.2015.00029

Scharff, L., Hort, M., & Gerst, A. (2014). The dynamics of the dome at Santiaguito volcano, Guatemala. *Geophysical Journal International*, *197*(2), 926–942. https://doi.org/10.1093/gji/ggu069

Scott, J. A. J., Mather, T. A., Pyle, D. M., Rose, W. I., & Chigna, G. (2012). The magmatic plumbing system beneath Santiaguito Volcano, Guatemala. *Journal of Volcanology and Geothermal Research*, *237-238*, 54–68. https://doi.org/10.1016/j.jvolgeores.2012.05.014

Scott, J. A. J., Pyle, D. M., Mather, T. A., & Rose, W. I. (2013). Geochemistry and evolution of the Santiaguito volcanic dome complex, Guatemala. *Journal of Volcanology and Geothermal Research*, *252*, 92–107. https://doi.org/10.1016/j.jvolgeores.2012.11.011

Self, S., Wilson, L., & Nairn, I. A. (1979). Vulcanian eruption mechanisms. *Nature*, *277*(5696), 440–443. https://doi.org/10.1038/277440a0

Shaw, H. R. (1980). The fracture mechanisms of magma transport from the mantle to the surface. In R. B. Hargraves (Ed.), *Physics of Magmatic Processes* (pp. 201–264). Princeton: Princeton University Press. Retrieved from http://www.jstor.org/stable/j.ctt7zv460.9, https://doi.org/10.1515/9781400854493.201

Siratovich, P., Davidson, J., Villeneuve, M., Gravley, D., Kennedy, B., Cole, J., et al. (2012). Physical and mechanical properties of the Rotokawa Andesite from production wells Rk 27 _ L2, Rk 28 and Rk 30. *New Zealand Geothermal Workshop 19-21 November*, (November), 7.

Sparks, R. S. J. (1997). Causes and consequences of pressurisation in lava dome eruptions. *Earth and Planetary Science Letters*, *150*(3–4), 177–189. https://doi.org/10.1016/S0012-821X(97)00109-X

Spieler, O., Kennedy, B., Kueppers, U., Dingwell, D. B., Scheu, B., & Taddeucci, J. (2004). The fragmentation threshold of pyroclastic rocks. *Earth and Planetary Science Letters*, *226*(1–2), 139–148. https://doi.org/10.1016/j.epsl.2004.07.016

Stanchits, S., Vinciguerra, S., & Dresen, G. (2006). Ultrasonic velocities, acoustic emission characteristics and crack damage of basalt and granite. *Pure and Applied Geophysics*, *163*(5-6), 975–994. https://doi.org/10.1007/s00024-006-0059-5

Stoiber, R. E., & Rose, W. I. (1969). Recent volcanic and fumarolic activity at Santiaguito volcano, Guatemala. *Bulletin Volcanologique*, *33*(2), 475–502. https://doi.org/10.1007/BF02596520

Suzuki-Kamata, K., Kusano, T., & Yamasaki, K. (2009). Fractal analysis of the fracture strength of lava dome material based on the grain size distribution of block-and-ash flow deposits at Unzen Volcano, Japan. *Sedimentary Geology*, *220*(3–4), 162–168. https://doi.org/10.1016/j.sedgeo.2009.04.026

Thomas, M. E., & Neuberg, J. W. (2012). What makes a volcano tick—A first explanation of deep multiple seismic sources in ascending magma. *Geology*, *40*(4), 351–354. https://doi.org/10.1130/G32868.1

Thomas, M. E., & Neuberg, J. W. (2014). Understanding which parameters control shallow ascent of silicic effusive magma. *Geochemistry, Geophysics, Geosystems*, *15*, 4481–4506. https://doi.org/10.1002/2014GC005529

Tuffen, H., Dingwell, D. B., & Pinkerton, H. (2003). Repeated fracture and healing of silicic magma generate flow banding and earthquakes? *Geology*, *31*(12), 1089. https://doi.org/10.1130/G19777.1

Voight, B., Hoblitt, R. P., Clarke, A. B., Lockhart, A. B., Miller, A. D., Lynch, L., & McMahon, J. (1998). Remarkable cyclic ground deformation monitored in real-time on Montserrat, and its use in eruption forecasting. *Geophysical Research Letters*, *25*(18), 3405–3408. https://doi.org/10.1029/98GL01160

Wadge, G., Ryan, G., & Calder, E. S. (2009). Clastic and core lava components of a silicic lava dome. *Geology*, *37*(6), 551–554. https://doi.org/10.1130/G25747A.1

Wadsworth, F. B., Witcher, T., Vasseur, J., Dingwell, D. B., & Scheu, B. (2017). When does magma break? In *Advances in Volcanology* (pp. 171–184). Cham: Springer International Publishing. https://doi.org/10.1007/11157_2017_23

Wadsworth, F. B., Witcher, T., Vossen, C. E. J., Hess, K.-U., Unwin, H. E., Scheu, B., et al. (2018). Combined effusive-explosive silicic volcanism straddles the multiphase viscous-to-brittle transition. *Nature Communications*, *9*(1), 1–8. https://doi.org/10.1038/s41467-018-07187-w

Walker, J. A., Singer, B. S., Jicha, B. R., Cameron, B. I., Carr, M. J., & Olney, J. L. (2011). Monogenetic, behind-the-front volcanism in southeastern Guatemala and western El Salvador: ^{40}Ar/^{39}Ar ages and tectonic implications. *Lithos*, *123*(1–4), 243–253. https://doi.org/10.1016/j.lithos.2010.09.016

Wallace, P. A., Kendrick, J. E., Miwa, T., Ashworth, J. D., Coats, R., Utley, J. E. P., et al. (2019). Petrological architecture of a magmatic shear zone: A multidisciplinary investigation of strain localisation during magma ascent at Unzen Volcano, Japan. *Journal of Petrology*, *60*(4), 791–826. https://doi.org/10.1093/petrology/egz016

Wei, X. X., & Chau, K. T. (2013). Three dimensional analytical solution for finite circular cylinders subjected to indirect tensile test. *International Journal of Solids and Structures*, *50*(14–15), 2395–2406. https://doi.org/10.1016/j.ijsolstr.2013.03.026

Xia, K., Rosakis, A. J., & Kanamori, H. (2004). Laboratory earthquakes: The sub-Rayleigh-to-supershear. *Science*, *303*(5665), 1859–1861. https://doi.org/10.1126/science.1094022

Yamamoto, H., Watson, I. M., Phillips, J. C., & Bluth, G. J. (2008). Rise dynamics and relative ash distribution in vulcanian eruption plumes at Santiaguito Volcano, Guatemala, revealed using an ultraviolet imaging camera. *Geophysical Research Letters*, *35*, L08314. https://doi.org/10.1029/2007GL032008

Zhang, D., Ranjith, P. G., & Perera, M. S. A. (2016). The brittleness indices used in rock mechanics and their application in shale hydraulic fracturing: A review. *Journal of Petroleum Science and Engineering*, *143*, 158–170. https://doi.org/10.1016/j.petrol.2016.02.011

Zorn, E. U., Rowe, M. C., Cronin, S. J., Ryan, A. G., Kennedy, L. A., & Russell, J. K. (2018). Influence of porosity and groundmass crystallinity on dome rock strength: A case study from Mt. Taranaki, New Zealand. *Bulletin of Volcanology*, *80*(4). https://doi.org/10.1007/s00445-018-1210-8